LASER SPECTROSCOPIC STUDIES OF IONS IN SOLIDS

By

ALI MUHAMMAD GHAZZAWI

Bachelor of Science
The American University of Beirut
Beirut, Lebanon
1978

Master of Science
The American University of Beirut
Beirut, Lebanon
1980

Submitted to the Faculty of the Graduate College
of the Oklahoma State University
in partial fulfillment of the requirements
of the Degree of
DOCTOR OF PHILOSOPHY
December, 1984

LASER SPECTROSCOPIC STUDIES OF IONS IN SOLIDS

Thesis Approved:

Richard C. Powell
Thesis Adviser

Burr J. Ackerman

E. J. Mc Guire

Larry E. Hallibrton

Norman N. Durham
Dean of the Graduate College

ACKNOWLEDGMENTS

In the first place, I must thank God for all the help and strength He has given me in my endeavors to accomplish this work. The help and guidance of my thesis adviser, Dr. Richard C. Powell, are gratefully acknowledged. I extend my thanks and gratitude to Dr. G. E. Venikouas and Dr. J. K. Tyminski for their assistance, and also to the members of the Graduate Committee: Dr. L. E. Halliburton, Dr. B. J. Ackerson, and Dr. G. J. Mains. I appreciate the financial support of the Physics Department, Oklahoma State University, and that of the National Science Foundation.

TABLE OF CONTENTS

LIST OF TABLES

Table Page

LIST OF FIGURES

CHAPTER I

INTRODUCTION

An important and effective tool in optical spectroscopy has emerged, viz. the laser. The variety in the types of lasers (solid-state, dye, gas) with their multifarious characteristics set Laser Spectroscopy in the front to serve in probing the physical properties of materials (in the three states of matter), especially those (to be) classified as laser materials.

In Chapter II of this thesis, laser excited time-resolved site-selection spectroscopy technique is utilized to study the results of the fluorescence properties of Eu^{2+} ions in $RbMgF_3$ crystals. The emission of these ions in different types of crystal field sites is identified and the energy transfer between ions in non-equivalent sites is characterized. The results indicate that the Eu^{2+} ions are forming clusters in this host.

Four-wave mixing (FWM) technique is implemented to investigate the nonlinear properties of alexandrite crystals. The FWM signal efficiency and decay rate were measured as functions of pump beam crossing angle, wavelength, and power. Chromium (Cr^{3+}) ions in alexandrite exist in both inversion and mirror sites, and gratings corresponding to both types of sites are established by varying the excitation wavelength. This study is presented in Chapter III.

Chapter IV deals with the study of exciton migration in neodymium pentaphosphate (NdP_5O_{14}) stoichiometric crystal employing nondegenerate

FWM technique. By tuning the excitation wavelength from the high energy side down to the low energy side into the absorption band, and for low and room temperature data no mobility edge is found in this material. The migration of energy is diffusive in all of the absorption band.

Finally, an Appendix on thermal gratings is provided since FWM transient-grating technique has been employed to observe them. Moreover, thermal gratings will be the subject of future research in alexandrite.

CHAPTER II

ENERGY MIGRATION STUDY IN $RbMgF_3:Eu^{2+},Mn^{2+}$ CRYSTALS

A. Introduction

The fluorescence properties of divalent europium ions in various host materials have been studied extensively for many years [1,2]. The two major reasons for the interest in this ion are its practical application as an X-ray intensifying phosphor and the fact that its spectral properties are highly sensitive to its local surroundings. This latter property makes Eu^{2+} an excellent probe of local crystal fields in different hosts. Recently, there has been a significant amount of interest in characterizing the defect structure of doped alkali halide crystals. Ions such as Eu^{2+} and Mn^{2+} have been used to study the effects of charge compensation, impurity aggregation, and precipitation of impurity phases [3-7]. It has been shown that the defect structure effects many of the important physical properties of these crystals. This type of work is now being extended to other types of crystals such as $RbMgF_3$ [8]. In this chapter, we describe the results of a study of the fluorescence properties of Eu^{2+} ions in $RbMgF_3$ crystals using laser excited, time-resolved site-selection spectroscopy techniques. Emission of Eu^{2+} ions in different types of crystal field sites is identified and the energy transfer between ions in non-equivalent sites is characterized. The results clearly indicate that

the Eu^{2+} ions are forming clusters in this host.

A recent investigation of the optical properties of this sample has shown that the Eu^{2+} and Mn^{2+} ions tend to form pairs, and that the excited Eu^{2+} ions in these pairs transfer virtually all of their energy to the Mn^{2+} ions [8]. Therefore, the Eu^{2+} ions which are paired with Mn^{2+} ions do not exhibit any fluorescence and the observed Eu^{2+} emission comes from ions which are not interacting with Mn^{2+}. This is verified by the fact that the measured Eu^{2+} fluorescence lifetime is not quenched by the addition of higher concentrations of Mn^{2+} ions. Therefore, in this study the presence of the Mn^{2+} ions in the crystal is essentially neglected since it does not affect the interaction between the Eu^{2+} ions, which is the main focus of this chapter.

B. Theoretical Background

Upon subjecting a material to (electromagnetic) radiation, certain types of ions or atoms are excited and may later release this excitation energy in the form of heat or light. During the period between excitation and dissipation, this energy may migrate within the material from one ion or atom (sensitizer) to another ion or atom (activator). This energy transfer may be accomplished either radiatively or non-radiatively. The former comprises the emission of light by the sensitizer ion and its subsequent receiving by the activator ion. This type of transfer has no effect on the fluorescence lifetime of the sensitizer.

On the other hand, non-radiative energy transfer processes shorten the fluorescence lifetime of the sensitizer, weaken its fluorescence intensities, and deplete the population of its excited states.

The sensitizer-to-activator transfer of energy can occur via electromagnetic multipole-multipole interaction or exchange interaction. Single-step energy transfer takes place whenever the sensitizer transfers its energy directly to the activator. However, multistep energy transfer mechanism may occur in the case when the sensitizer transfers the energy to one or more other sensitizers before the activator finally receives it. The latter mechanism is likely to take place when the concentration of sensitizers is sufficiently high, in contrast to the sample investigated in this study.

Whenever a mismatch in energy between the transitions of sensitizer and activator exists, phonon-assisted energy transfer processes are likely to arise. The energy transfer rates, then, depend on the size of this energy mismatch. These processes are temperature dependent and involve considering the ion-ion and electron-phonon interactions. These processes are not considered in this study, however.

C. Resonant Single-Step Energy Transfer

Resonant transfer of energy from sensitizer s to activator a may arise when there are no differences in energy between the ground and excited states of both ions, i.e., no energy mismatch between the transitions of s and a. With appropriate interaction between the electronic systems of the sensitizer and activator, energy transfer to the latter takes place. Förster [9] and Dexter [10] derived expressions of energy transfer rates arising from multipole-multipole and exchange interactions employing time-dependent perturbation theory formalism.

Consider a system in which initially the sensitizer ion is in the excited state ψ_s^* and the activator ion is in the ground state ψ_a. The

electrostatic interaction Hamiltonian (analogous to that of van der Waals) is written as

$$H_{int}^{ES} = \sum_{i,j} \frac{e^2/\varepsilon}{|\vec{r}_{s_i} - \vec{r}_{a_j} - \vec{R}_{sa}|} \tag{1}$$

Here, $\vec{r}_{s_i}$ and $\vec{r}_{a_j}$ are the coordinate vectors of electrons i and j belonging to ions s and a, respectively, R_{sa} is the sensitizer-activator separation, and ε is the dielectric constant of the host crystal. The denominator can be expanded in a Taylor series about R_{sa} and, thereby one obtains the leading terms corresponding to electric dipole-dipole (DD), dipole-quadrupole (DQ), and quadrupole-quadrupole (QQ) interactions with the radial dependence R_{sa}^{-3}, R_{sa}^{-4}, and R_{sa}^{-5} respectively.

On the other hand, the exchange interaction Hamiltonian arising from the overlap of charge clouds of electrons on the sensitizer and activator may be represented by

$$H_{int}^{EX} = \sum_{i,j} - J_{ij} \vec{s}_i \cdot \vec{s}_j \tag{2}$$

where J_{ij} is the exchange integral and $\vec{s}_i$ and $\vec{s}_j$ are the spin vectors of electrons i and j, respectively.

The energy transfer rate (probability/time) between the sensitizer and activator is given by the known expression

$$W_{sa} = \frac{2\pi}{\hbar} \rho_E \left| \langle \psi_i | \; H_{int} \; | \psi_f \rangle \right|^2 \tag{3}$$

where ψ_i and ψ_f are the initial and final antisymmetrized wave functions of the system, and ρ_E is the density of states. Equation (3) can be

written in terms of the line shape functions $g_s(E)$ and $g_a(E)$ as

$$W_{sa} = \frac{2\pi}{\hbar} \left|\langle \psi_s^* \psi_a \right| H_{int} \left| \psi_s \psi_a^* \rangle\right|^2 \int g_s(E)\, g_a(E)\, dE \qquad (4)$$

The integral is over the normalized emission band shape of the sensitizer and the absorption band of the activator with line shape functions $g_s(E)$ and $g_a(E)$ representing the transitions $s \rightarrow s^*$ and $a \rightarrow a^*$, respectively normalized according to $\int g(E)dE = 1$.

Using equation (4), the electric dipole-dipole energy transfer rate is expressed as [11]

$$W_{sa}^{DD} = \frac{3}{4}\left(\frac{e^2}{mc^2}\right) \frac{\phi_s\, f_a}{(2\pi n\, \tilde{\nu}_{sa})^4} \frac{1}{\tau_s^o\, R_{sa}} \int g_s(\tilde{\nu})\, g_a(\tilde{\nu})\, d\tilde{\nu} \qquad (5)$$

where f_a is the oscillator strength of the activator transition, ϕ_s is the quantum efficiency of the sensitizer, n is the index of refraction of the host material, τ_s^o is the intrinsic fluorescence decay time of the sensitizer, and $\tilde{\nu}_{sa}$ is the average wave number in the region of spectral overlap. The transformation from $g(E)$ to $g(\tilde{\nu})$ is done through $E = (hc)\tilde{\nu}$. Denoting the overlap integral of the sensitizer and activator transitions by Ω , one defines a "critical interaction distance" R_o as

$$R_o = \left[\frac{3}{4}\left(\frac{e^2}{mc^2}\right) \frac{\phi_s\, f_a \Omega}{(2\pi n\, \tilde{\nu}_{sa})^4}\right]^{1/6} \qquad (6)$$

and obtains a "critical transfer concentration"

$$C_o = \left(\frac{4}{3}\,\pi\, R_o^3\right)^{-1} \qquad (7)$$

Consequently, the dipole-dipole energy transfer rate expression in equation (5) reduces to [9]

$$W_{sa}^{DD} = (\tau_s^o)^{-1} (R_o / R_{sa})^6 \tag{8}$$

Remark that $R_o = R_{sa}$ when $W_{sa}^{DD} = (\tau_s^o)^{-1}$ which defines the critical interaction distance as the sensitizer-activator separation that corresponds to an energy transfer rate equal to the intrinsic decay rate of the sensitizer.

For multipole-multipole interaction, the population (density) of the excited sensitizers is found to be [9-11]

$$n_s(t) = n_s(0) \exp\left\{\frac{-t}{\tau_s^o} - \Gamma\left(1-\frac{3}{m}\right)\left(\frac{C_a}{C_o}\right)\left(\frac{t}{\tau_s^o}\right)^{\frac{3}{m}}\right\} \tag{9}$$

where C_a is the concentration of the activator, and m = 6, 8, and 10 for electric dipole-dipole, dipole-quadrupole, and quadrupole-quadrupole interaction respectively.

The energy transfer rate for the exchange interaction mechanism is given by [10]

$$W_{sa}^{EX} = \frac{2\pi}{h} K^2 \exp\left(\frac{-2R_{sa}}{L}\right) \int g_s(E)\, g_a(E)\, dE \tag{10}$$

where K is a constant involving the overlap of the electron wave functions and having the dimension of energy, and L is the effective average Bohr radius. Assuming hydrogen-like wave functions simplifies the above expression to [10,12]

$$W_{sa}^{EX} = (\tau_s^o)^{-1} \exp[\gamma(1 - \frac{R_{sa}}{R_o})] \tag{11}$$

where $\gamma = 2R_o/L$.

For an ensemble of sensitizers and activators experiencing exchange interaction, the population of the excited sensitizers is given by [12]

$$n_s(t) = n_s(0) \exp[\frac{-t}{\tau_s^o} - \gamma^{-3} (\frac{C_a}{C_o}) g(e^{\gamma} \frac{t}{\tau_s^o})] \tag{12}$$

where

$$g(z) = -z \int_0^1 \exp(-zy)(\ln y)^3 \, dy$$

In deriving the above expression, the interaction among sensitizers and back transfer from activators to sensitizer were not included.

D. Experimental

Good optical quality single crystals of $RbMgF_3$ were grown by the Bridgeman method in the Oklahoma State University Crystal Growth Facility. The sample investigated here was doped with about 0.05% Eu^{2+} and about 0.15% Mn^{2+}. The polished sample was mounted on the cold finger of an Air Products and Chemicals Model CS-202 Displex Cryogenic (closed-cycle helium) Refrigerator capable of attaining temperatures between 12 K and 300 K.

The experimental setup for time-resolved spectroscopy and lifetime measurements is depicted in Figure 1. A Molectron UV-14 pulsed nitrogen laser was used as the excitation source. This produced a pulse of about

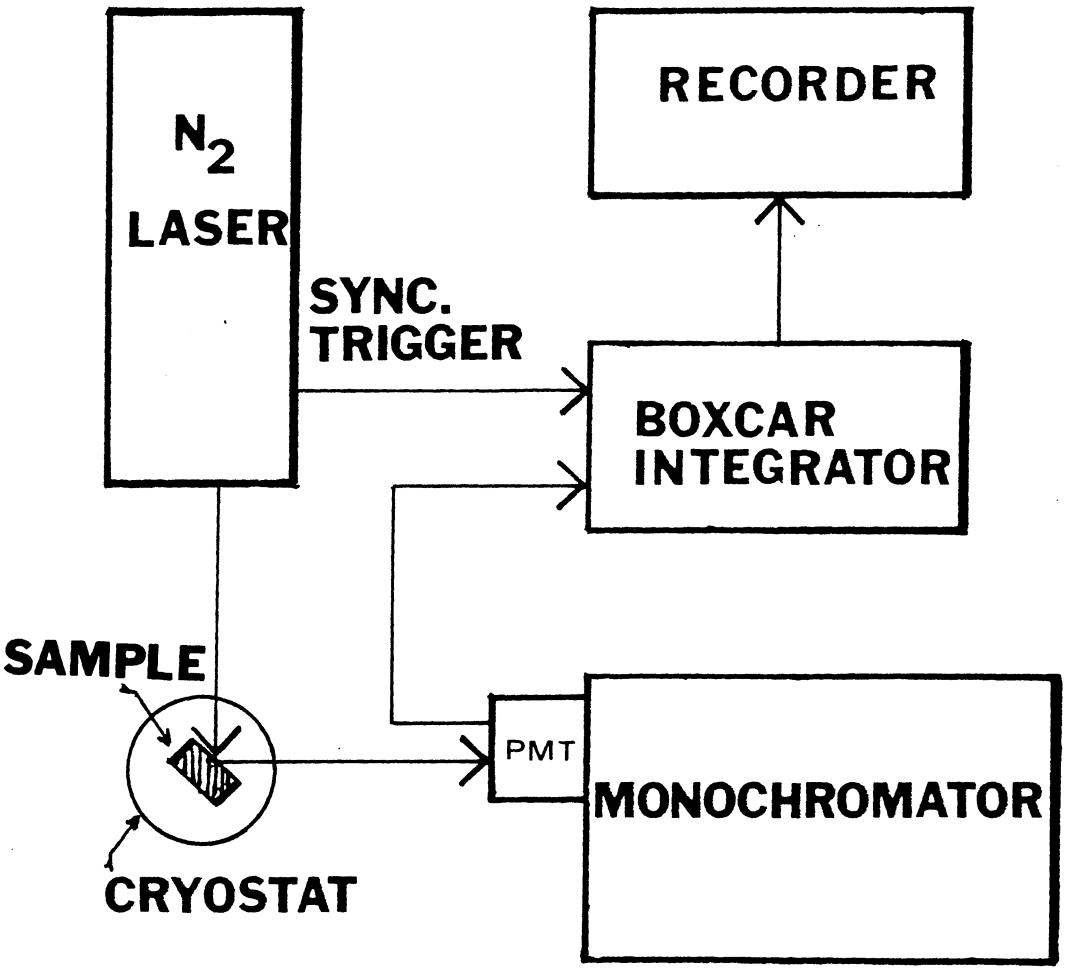

Figure 1. Experimental setup for Time-Resolved Spectroscopy and lifetime measurements.

10 nsec in duration and 1 Å bandwidth at 3371 Å . The sample fluorescence was focused on the entrance slit of a Spex 1-m Czerny-Turner monochromator model 1704 set for a resolution of 0.3 Å (dispersion = 4 Å /mm and slit width = 0.70 mm). The fluorescence signal was detected by a cooled RCA C31034 photomultiplier tube. A Princeton Applied Research (PAR) Model 162 Boxcar Integrator, supplemented by a Model 165 gated integrator processor module, was implemented to sample and average the signal. The time resolution for the system was set at 15 nsec.

For time-resolved spectroscopy measurements, a time aperture was set at a fixed time after the laser pulse and the monochromator was scanned over a certain range of wavelengths ensuing in a spectrum of the sample fluorescence. On the other hand, the aperture was scanned in time to measure the fluorescence decay time with the monochromator set at a specific wavelength. In each case, the resulting output was recorded on a strip chart recorder and an input load resistor was used to avoid the distortion of the signal by the response of the system. Furthermore, an LSI-11 computer was utilized in fitting the required data.

The energy level diagram for Eu^{2+} ion is given in Figure 2. The laser pulse excites the $^8S_{7/2} \rightarrow {}^6P_{7/2}$ transition within the $4f^7$ configuration of Eu^{2+}. The inverse of this transition is the origin of the fluorescence emission in this host, whose structure [13] is shown in Figure 3. However, recent investigations imply that the F^- ions are farther than illustrated.

E. Data and Interpretation

The fluorescence emission of the Eu^{2+} ions at 12 K at various times

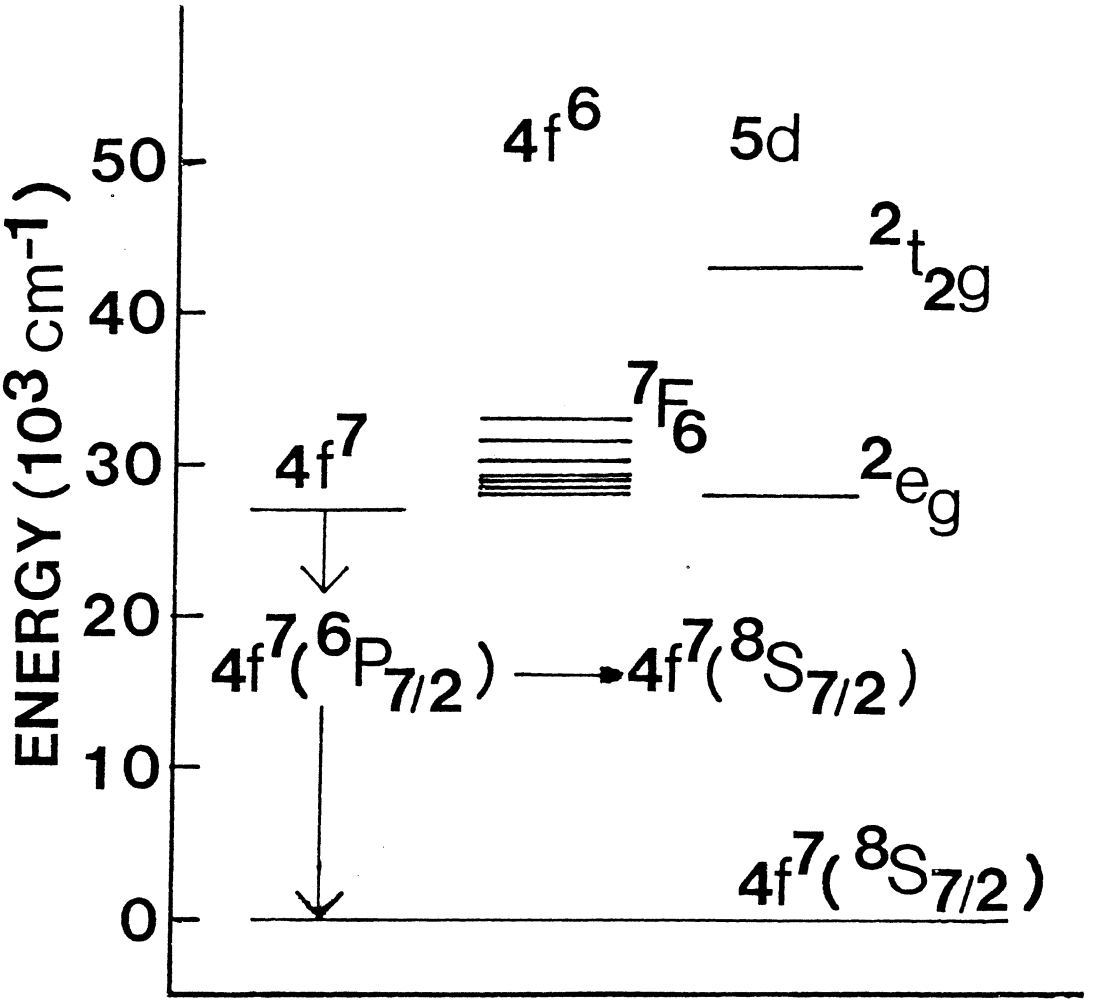

Figure 2. The energy level diagram for the Eu^{2+} ion in $RbMgF_3$ crystals.

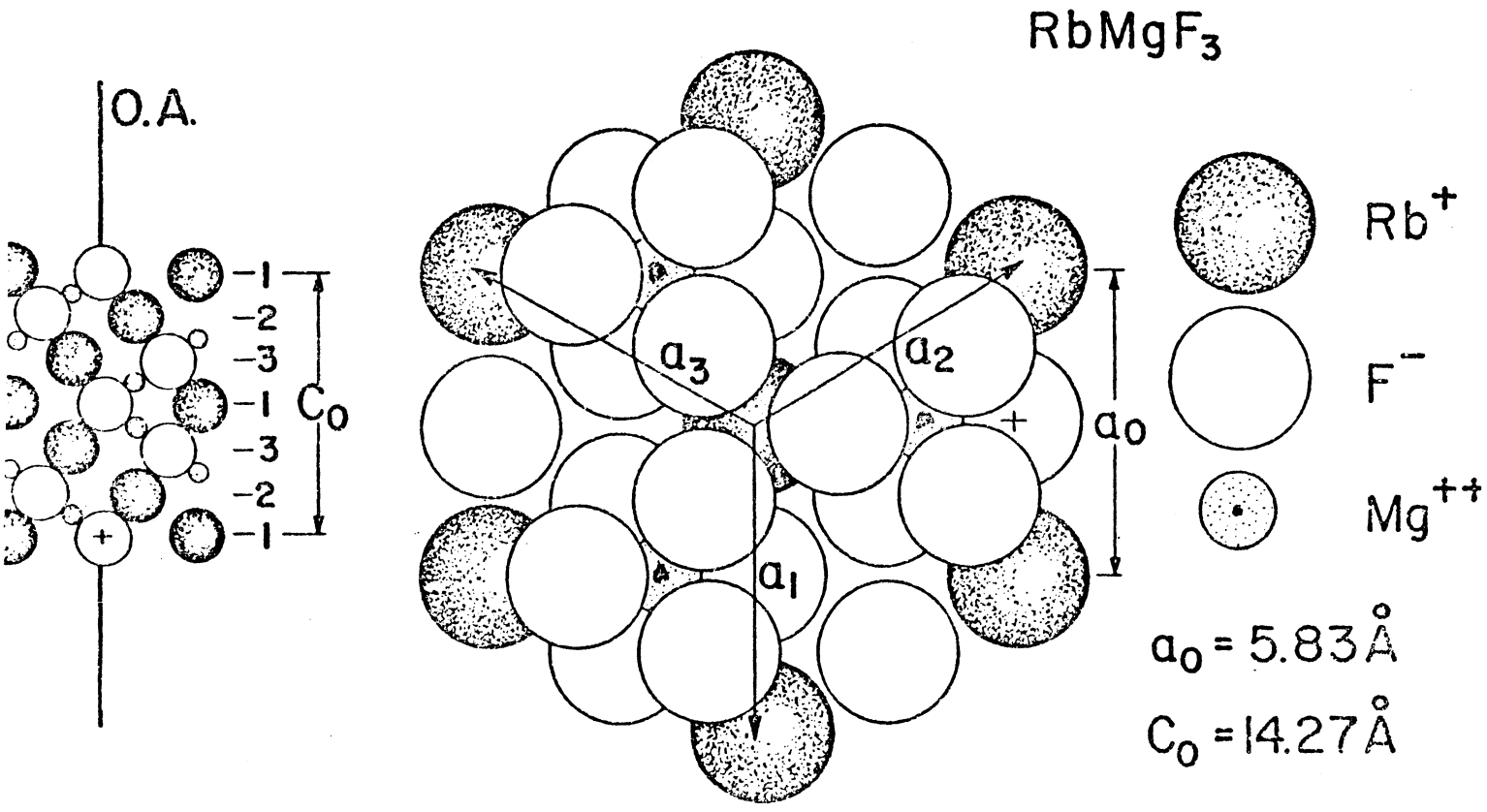

Figure 3. The crystal structure of $RbMgF_3$ crystal with the optic axis parallel to the c_o-axis [13].

after the laser pulse was taken. Figure 4 shows the emission at 1 μs and 50 μs after the excitation pulse. Two prominent spectral lines show up dominantly with some less intense structure. The strong line at 3605.4 Å is the most intense at short times and the strong line at 3613.8 Å is the most intense at long times. Both of these lines are attributed to the same transition of Eu^{2+} ions in slightly different crystal field sites which have different energy level splittings. The splitting [14] of the ground state $^8S_{7/2}$ is about 0.2 cm^{-1} and hence too small to be observed. The weak structure on the higher energy side of each of the main lines is due to transitions from the higher crystal field multiplets of the $^6P_{7/2}$ level and from ions in other less populated types of crystal field sites. The observed time dependence indicates that energy transfer is taking place from ions giving rise to the high energy line to the ions in sites producing the low energy line. Thus, these lines are labeled sensitizer (s) and activator (a), respectively. The lifetime of the former is measured to be 50.09 μs and that of the latter is 103.84 μs, and are listed in Table I.

In order to quantitatively characterize the dynamics of the energy transfer process, the ratio of the integrated intensities of the activator to the sensitizer lines was plotted versus time after the laser pulse as shown in Figure 5. Table II lists the corresponding points. There is a rapid increase at short times and then a leveling off at longer times indicating that some equilibrium condition has been reached.

In order to interpret the energy transfer data, a model involving the interaction of two two-level systems is assumed as shown in Figure 6. The rate equations describing the dynamics of the excited state

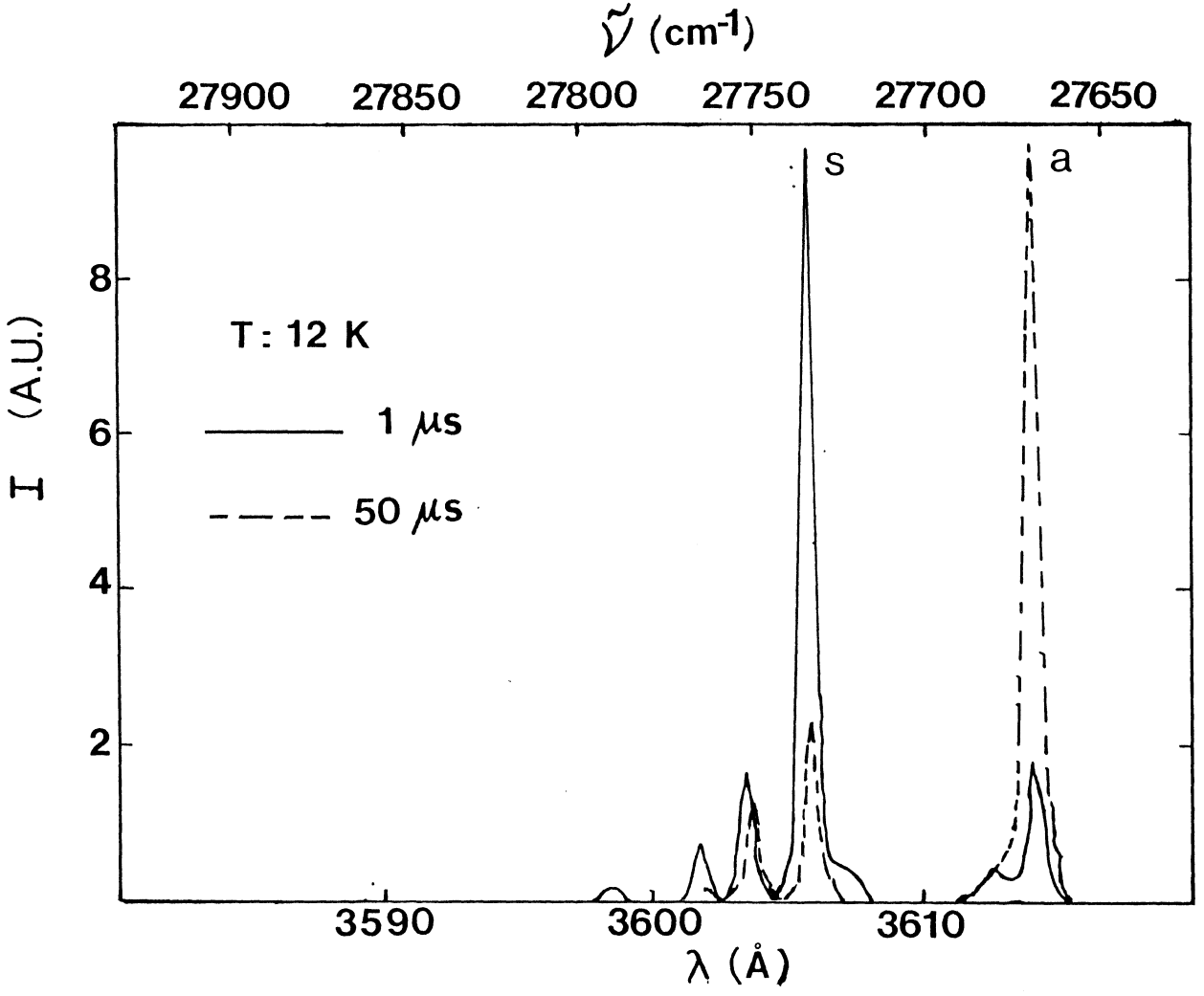

Figure 4. Eu^{2+} emission spectra at 12 K at two times after the excitation pulse.

TABLE I

ENERGY TRANSFER PARAMETERS

Parameter	T(K) 12		77
τ_s(μs)	50.09		20.7
τ_a(μs)	103.84		693.0
$W_{sa}(s^{-1})$	6.16×10^4		
$W_{as}(s^{-1})$	0.90×10^4		
$n_a(0)/n_s(0)$	0.25		
β_s^r/β_a^r	1.15		
R_o(Å)	7.8		9.0
R_{sa}(Å)	6.5		9.0
τ_r(μs)		50.1	
W_t^{-1}(μs)		15.4	
W_p^{-1}(ms)		1.0	
$\Delta E_t(cm^{-1})$		31.25	
$\Delta E_p(cm^{-1})$		34.27	

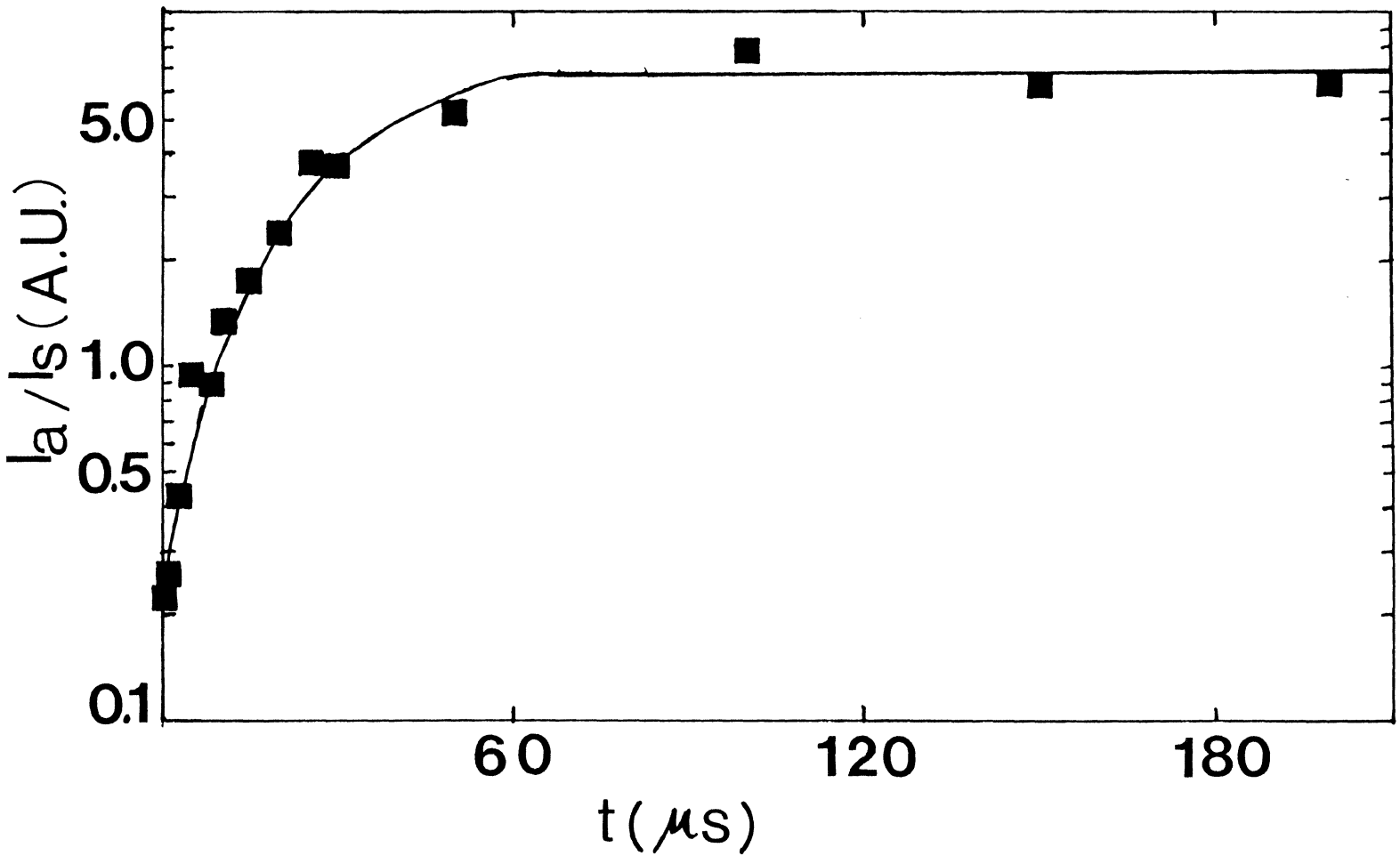

Figure 5. Ratio of the integrated fluorescence intensities as a function of time after the excitation pulse at 12 K. The solid line is the theoretical fit to the data.

TABLE II

RATIO OF INTEGRATED INTENSITIES AS A FUNCTION OF TIME AFTER THE LASER PULSE AT T = 12 K

t(μs)	Experimental I_a/I_s	Theoretical Fit I_a/I_s
0.5	0.23	0.25
1.0	0.26	0.28
2.5	0.43	0.39
5.0	0.94	0.60
7.5	0.91	0.83
10.0	1.34	1.09
15.0	1.77	1.69
20.0	2.40	2.38
25.0	3.82	3.12
30.0	3.82	3.84
50.0	5.20	5.91
100.0	7.80	6.78
150.0	6.50	6.80
200.0	6.50	6.80

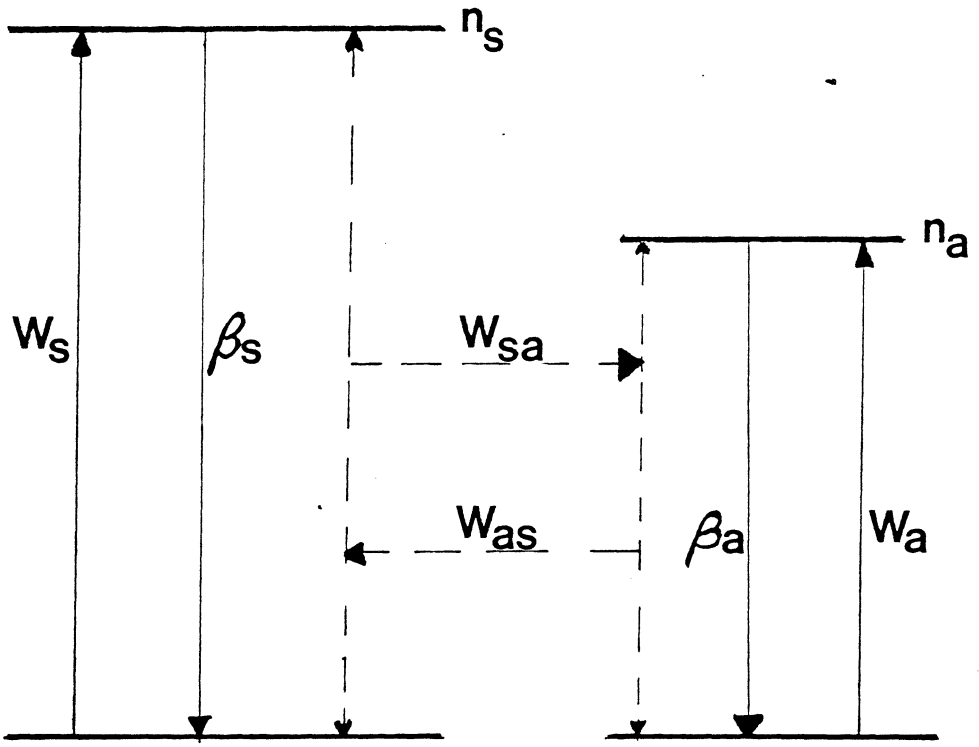

Figure 6. Two-level system model for energy transfer in $RbMgF_3:Eu^{2+},Mn^{2+}$ crystal.

populations are

$$\dot{n}_s(t) = n_s(0)\delta(t) - (\beta_s + W_{sa})\, n_s(t) + W_{sa}\, n_a(t) \tag{13}$$

$$\dot{n}_a(t) = n_a(0)\delta(t) - (\beta_a + W_{as})\, n_a(t) + W_{as}\, n_s(t) \tag{14}$$

where $n_s(t)$ and $n_a(t)$ are the populations of the excited states of sensitizers and activators at time t, respectively, β_s and β_a are the fluorescence decay rates of the ions in the two types of sites, and W_{sa} and W_{as} are the energy transfer and back transfer rates. The excitation pulse is approximated by a $\delta(t)$- function. The excited state populations are related to the measured fluorescence intensities by $I_i = \beta_i^r n_i$ where β_i^r represents the radiative decay rate.

By Laplace transforming both sides of equations (13) and (14) and dividing them, the solution comes out as

$$\frac{I_a(t)}{I_s(t)} = \frac{I_a(0)}{I_s(0)} \left(\frac{1 + G_a \tanh Bt}{1 + G_s \tanh Bt}\right) \tag{15}$$

where

$$B^2 = \frac{1}{4}(W_{sa} + \beta_s - W_{as} - \beta_a)^2 + W_{sa}\, W_{as}$$

and

$$G_a = B^{-1}\left[\frac{n_s(0)}{n_a(0)} W_{sa} + \frac{1}{2}(W_{sa} + \beta_s - W_{as} - \beta_a)\right]$$

$$G_s = B^{-1}\left[\frac{n_a(0)}{n_s(0)} W_{as} - \frac{1}{2}(W_{sa} + \beta_s - W_{as} - \beta_a)\right]$$

Equation (15) was used to obtain the best fit to the data assuming as time-independent adjustable parameters the energy transfer rates W_{sa} and W_{as}, the initial population ratio $n_a(0)/n_s(0)$, and the ratio of the radiative decay rates β_a^r/β_s^r. The theoretical fit is denoted by the solid line in Figure 5 and the various fitted parameters are listed in Table I.

As the temperature is raised, the Eu^{2+} emission spectrum becomes much more complex. This is due partially to emission from thermally populated upper components of the crystal field split metastable state manifold. In addition, the population of new levels and the presence of thermal energy cause the activation of energy transfer to Eu^{2+} ions in new types of sites. A portion of the Eu^{2+} emission spectrum at 77 K is shown in Figure 7 at two times after the excitation pulse. The sensitizer line at 3605.4 Å still is strongly selectively excited, but now emission can also be observed from the next higher crystal field component of the metastable state of the ions in this type of site. This appears as the line at 3601.2 Å in the spectrum, which implies a crystal field splitting of $\Delta E = 32.4\ cm^{-1}$. The activator line identified at low temperature is weak and shows little relative time dependence at high temperatures. This indicates that the ions in this type of site are no longer effective in receiving the energy from the ions in the sensitizer sites. Instead, the relative time evolution of the spectral line at 3603.0 Å indicates that the ions in the type of site producing this transition are being strongly pumped through energy transfer from the sensitizer ions. Although some of the spectral lines at higher energy may be associated with other transitions from these activator ions, the overlap among the various lines makes it formidable to have any

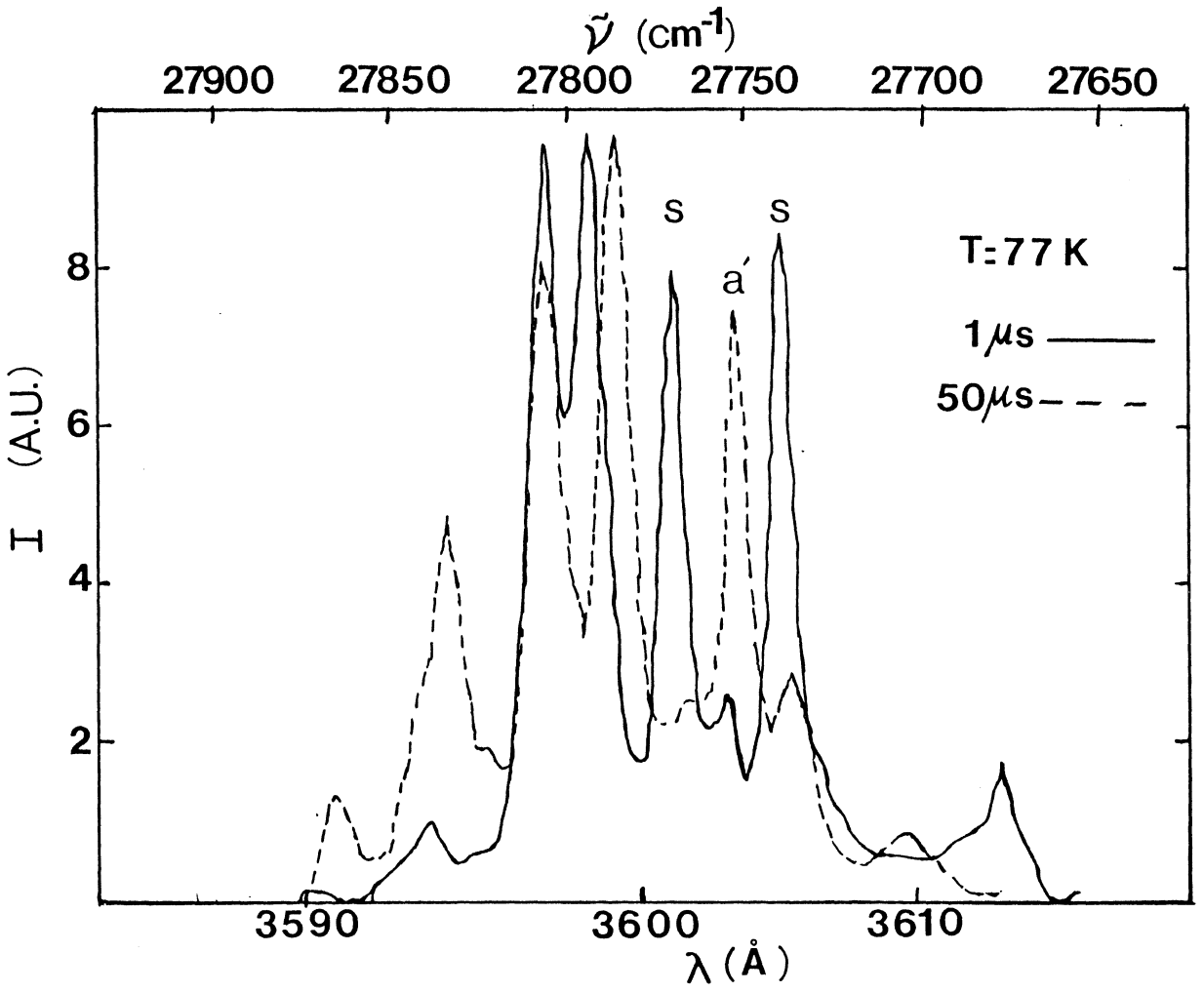

Figure 7. Eu^{2+} emission spectra at 77 K at two times after the excitation pulse.

definitive assignment.

The general form of the time dependence of the ratio of the integrated intensities of the sensitizer and activator transitions is similar to that observed at low temperatures. No attempt was made to quantitatively fit the high temperature time-resolved spectroscopy data with a two-level system model since the complex nature of the spectrum does not allow the lines to be resolved cleanly. Thus the error bars on the data were too large to obtain unique theoretical fits.

The evolution of the spectral characteristics with temperature from the 12 K and the 77 K values is very complex because of the presence of various different types of physical processes. For example, Figure 8 shows the change with temperature of the ratio of the integrated intensities of the sensitizer and both types of activator emissions at 1 μs after the excitation pulse. The high value of the ratio at low temperature is due to the quenching of the sensitizer fluorescence by energy tranfer to the low temperature type of activator ions. The ratio decreases as temperature is increased because this type of process is turning off. Table III lists the values of the ratio of the integrated intensities for various temperature values at 1 μs and 50 μs after the laser pulse.

Figure 9 also shows the changes in the fluorescence lifetimes with temperature. The low temperature activator emission quenches rapidly with temperature, whereas the sensitizer emission decreases rapidly at low temperature and begins to level out at high temperature. The high temperature activator lifetime exhibits a temperature behavior similar to that of the sensitizer. These changes again indicate the occurence of complex spectral dynamics. An example of one possible way to

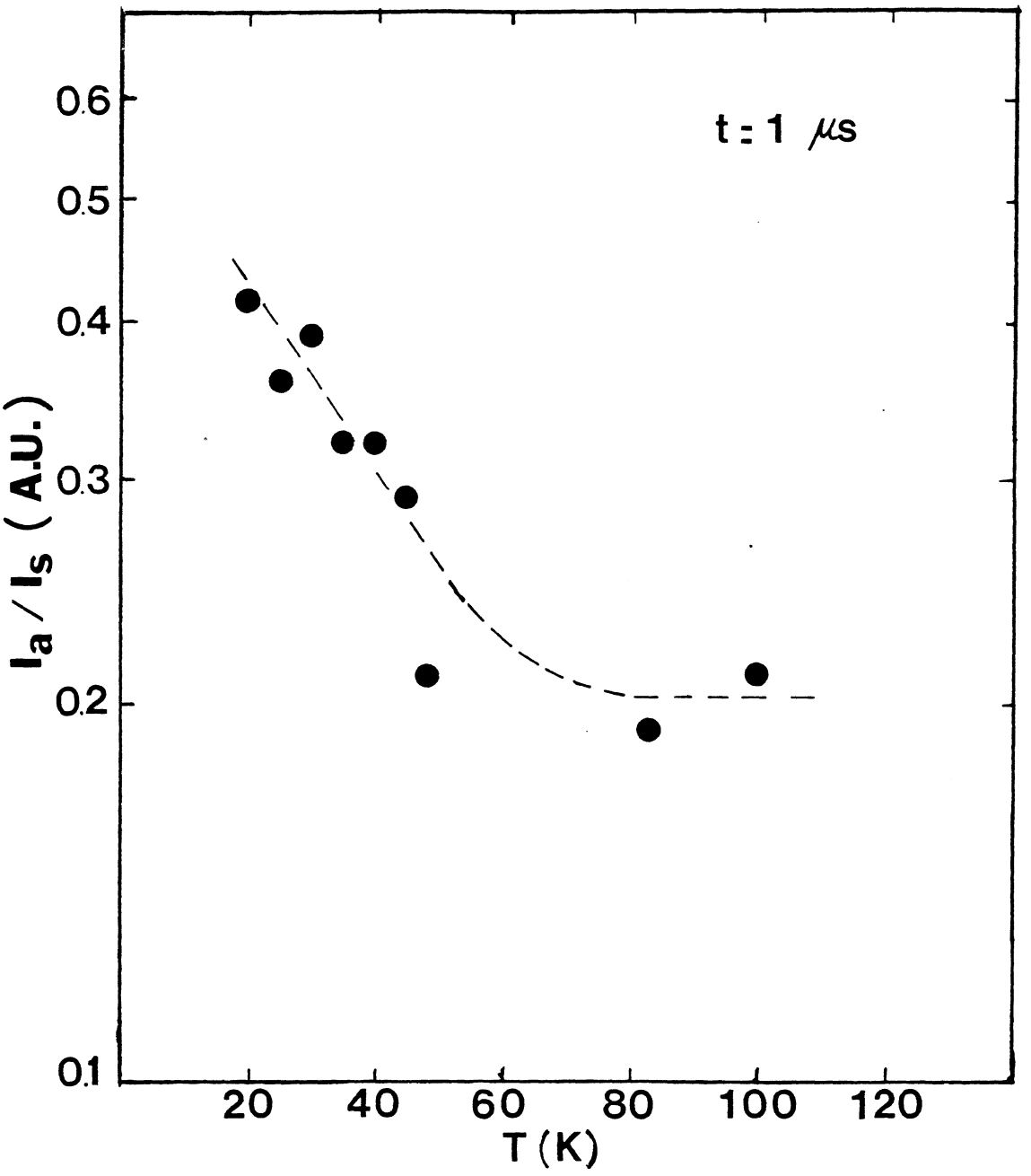

Figure 8. Temperature dependence of the fluorescence intensity ratios taken at 1.0 μs after the excitation pulse.

TABLE III

VARIATION OF THE RATIO OF THE INTEGRATED INTENSITIES WITH TEMPERATURE

	t = 1 μs	t = 50 μs
T(K)	I_a/I_s	I_a/I_s
20	0.43	4.06
25	0.36	1.20
30	0.39	0.97
35	0.32	1.01
40	0.32	1.02
45	0.29	0.97
48	0.21	1.48
83	0.19	1.22
100	0.21	1.30

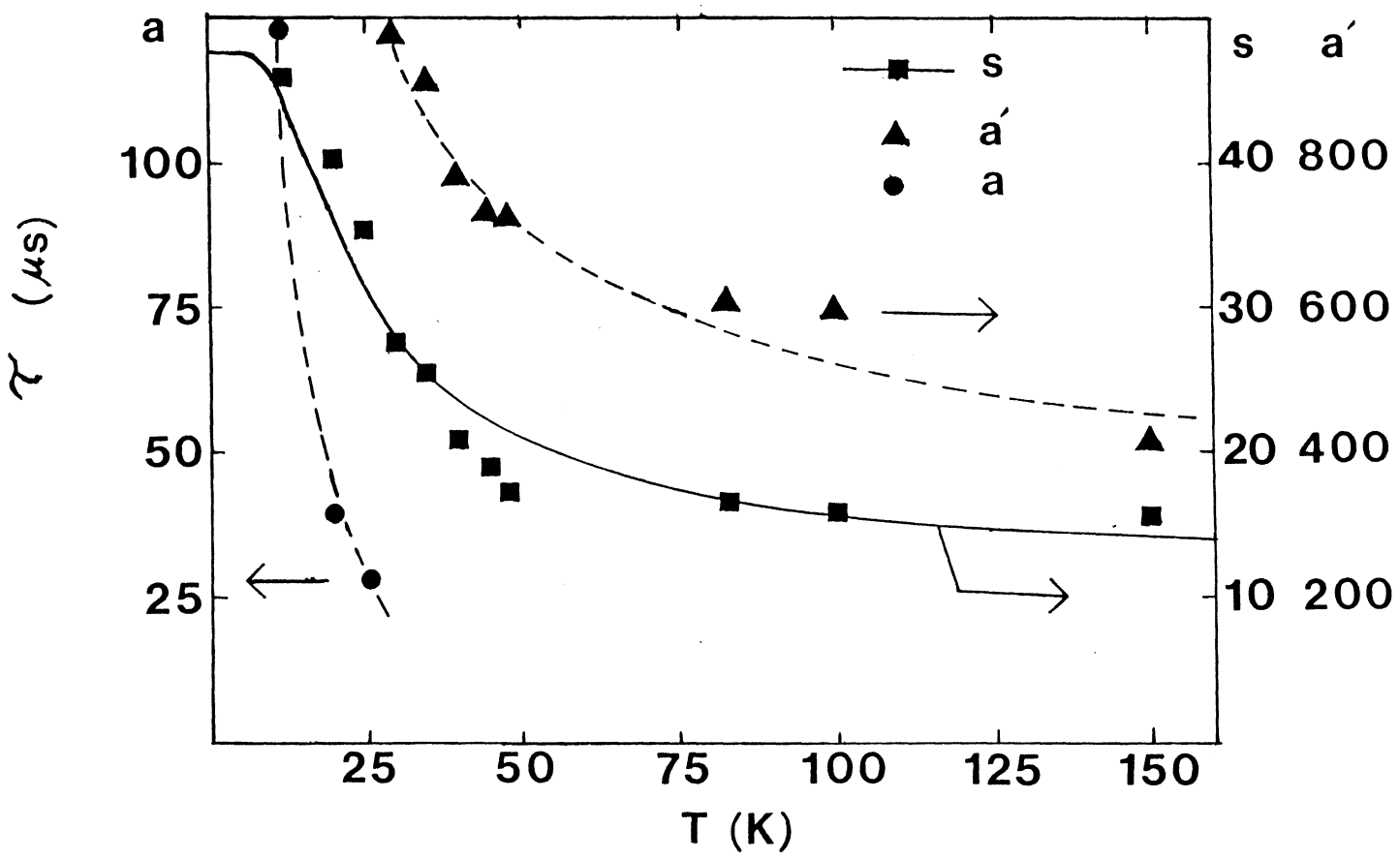

Figure 9. Temperature dependence of the fluorescence lifetimes of the sensitizer(s), low temperature activator (a), and high temperature activator (a´) ions. See the text for the explanation of the theoretical solid line.

interpret the temperature variation of the sensitizer decay time is through the equation

$$\tau_f^{-1} = \tau_r^{-1} + W_t\, e^{-\Delta E_t/kT} + W_p(1 - e^{-\Delta E_p/kT})^{-1} \qquad (16)$$

Here τ_f is the fluorescence decay time of these ions, τ_r is the radiative decay time, W_t is the energy transfer rate, and W_p is the phonon emission rate. The transfer process is assumed to occur with an exponential activation energy of ΔE_t. The phonon emission term helped in leveling off the fluorescence lifetime at high temperatures. The data for the sensitizer were fitted using equation (16) with W_t, W_p, τ_r, ΔE_t, and ΔE_p as adjustable parameters. The best fit to the data is represented by the solid line in Figure 9. The corresponding fitted parameters are listed in Table I. The data for the variation of the sensitizer's fluorescence lifetime with temperature are given in Table IV.

At 12 K the best fit to the time-resolved spectroscopy data was obtained using time-independent energy transfer rates. Attempts to obtain a good fit to the data with time-dependent rates were unsuccessful. Constant energy transfer rates indicate the presence of two possible physical situations. The first is transfer over fixed sensitizer-activator separations, and the second is transfer involving efficient migration of energy among the sensitizer ions before transfer to activators. The latter process is unlikely in this case because of the low concentration of sensitizer ions.

For constant sensitizer-activator separation R_{sa}, the energy transfer rate for electric dipole-dipole interaction can be expressed as

TABLE IV

VARIATION OF FLUORESCENCE LIFETIME OF THE SENSITIZER WITH TEMPERATURE

T(K)	Experimental Data τ_s(μs)	Theoretical fit τ_s(μs)
20	40.39	35.84
25	35.50	31.39
30	27.70	28.01
35	25.56	26.27
40	21.00	23.55
45	19.07	22.04
48	17.30	21.30
83	16.59	16.68
100	15.80	15.64
150	15.63	13.96

in equation (8), where the critical interaction distance R_o is given by equation (6) with the index of refraction of $RbMgF_3$ being 1.48. Assuming Lorentzian lines $g_a(\tilde{\nu})$ and $g_s(\tilde{\nu})$, the overlap integral Ω can be written as

$$\Omega = \int g_a(\tilde{\nu})\, g_s(\tilde{\nu})\, d\tilde{\nu} = \frac{1}{\pi} \frac{\Delta\tilde{\nu}_s + \Delta\tilde{\nu}_a}{(\Delta\tilde{\nu}_s + \Delta\tilde{\nu}_a)^2 + (\tilde{\nu}_s - \tilde{\nu}_a)^2} \tag{17}$$

where $\tilde{\nu}_i$ and $\Delta\tilde{\nu}_i$ are the positions and widths of the spectral transitions. Moreover, the oscillator strength of the activator transition f_a, assuming a Lorentz local type of field, is given by [15]

$$f_a = 1.51\, \tau_a^{-1}\, \lambda_a^2 / [(n^2 + 2)^2/9n] \tag{18}$$

Using the observed spectral parameters, the critical interaction distance is predicted to be 7.8 Å at 12 K and 9.0 Å at 77 K. If these values are substituted in equation (8) along with the measured fluorescence lifetimes and the energy transfer rates obtained respectively from fitting the time-resolved spectroscopy and fluorescence lifetime temperature variation data, the sensitizer-activator separations are found to be approximately 6.5 Å at 12 K and 9.0 Å at 77 K. The low temperature value is close to the nearest neighbor separation between Eu^{2+} sites which is 5.84 Å in $RbMgF_3$ crystals [16]. The high temperature value is close to the fifth nearest neighbor distance (9.6 Å).

Using equation (16), the transfer rate at 77 K was found to be about 4.7×10^4 sec^{-1}. The activation energy of 31.2 cm^{-1} is consistent with the measured splitting of 32.4 cm^{-1} between the two crystal field components of the sensitizers. The ratio of the back transfer to the

transfer rate should be proportional to a Boltzmann factor $\exp\{-\Delta E_{sa}/kT\}$. The data obtained at 12 K predicts a value of ΔE_{sa}=16.0 cm^{-1} which is close to the difference in the energies of the high energy activator level and the upper crystal field component of the sensitizer, 13.9 cm^{-1}.

CHAPTER III

FOUR-WAVE MIXING STUDY IN $BeAl_2O_4:Cr^{3+}$ CRYSTALS

A. Introduction

Four-wave mixing (FWM) is a useful spectroscopic tool enabling one to investigate properties of solids not obtainable by other methods. Moreover, it is one of the most used techniques to generate phase conjugate waves [17]. Degenerate four-wave mixing (DWFM) is a (FWM) process in which all the input and output waves (fields) have the same wavelength, and is the technique implemented in the study per se.

Two input waves interact in a material building up a grating arising from the change in the optical properties of the material. The nonlinear response of the latter may be described through the third-order (nonlinear) susceptibility $\chi^{(3)}$ as proposed by Yariv and Pepper [18]. Two-level [19,20], three-level [21], and equivalently two two-level systems [22] were suggested in attempt to interpret the coupling of the interacting fields. On the other hand, the grating diffracts a probe beam giving rise to four-wave mixing signals with scattering efficiency defined as the signal ratio of the latter to the former and not exceeding 10^{-2} in most (yet known) experiments. The physical processes responsible for establishing the gratings and/or washing them away are in themselves worthy of study. This can be done through utilizing FWM transient-grating spectroscopy technique [23].

Alexandrite, chromium doped $BeAl_2O_4$ crystal, has been studied by several researchers in terms of its use as a laser material [24-31]. In fact, very successful solid state tunable lasers depending on alexandrite crystals were developed [32]. However, the nonlinear properties of this material has not yet been completely studied. These properties can be important in determining device properties for high power laser operation.

In this chapter, we derive an expression of the diffraction efficiency of an optical wave from a (thick) grating assuming a simple coupled-wave analysis [33]. Then we present the data manifesting some properties of the FWM signal in alexandrite crystals and interpret the results in terms of excited-state population gratings of Cr^{3+} ions in different types of sites.

B. Theoretical Background

In a coupled wave theory treatment [33], a monochromatic light beam (e.g., of laser) R is Bragg incident on a grating of thickness d and is subsequently diffracted off leaving the medium (crystal, say) as signal wave S. Waves R and S are assumed to be transverse and interact with one another and are depicted in Figure 10. Perpendicular polarization of light to the plane of incidence (though not necessary) is assumed.

The total electric field is the superposition of the two waves and is given by

$$\vec{E} = \vec{R}(z)\, e^{-i\vec{k}_R \cdot x} + \vec{S}(z)\, e^{-i\vec{k}_S \cdot \vec{x}} \qquad (19)$$

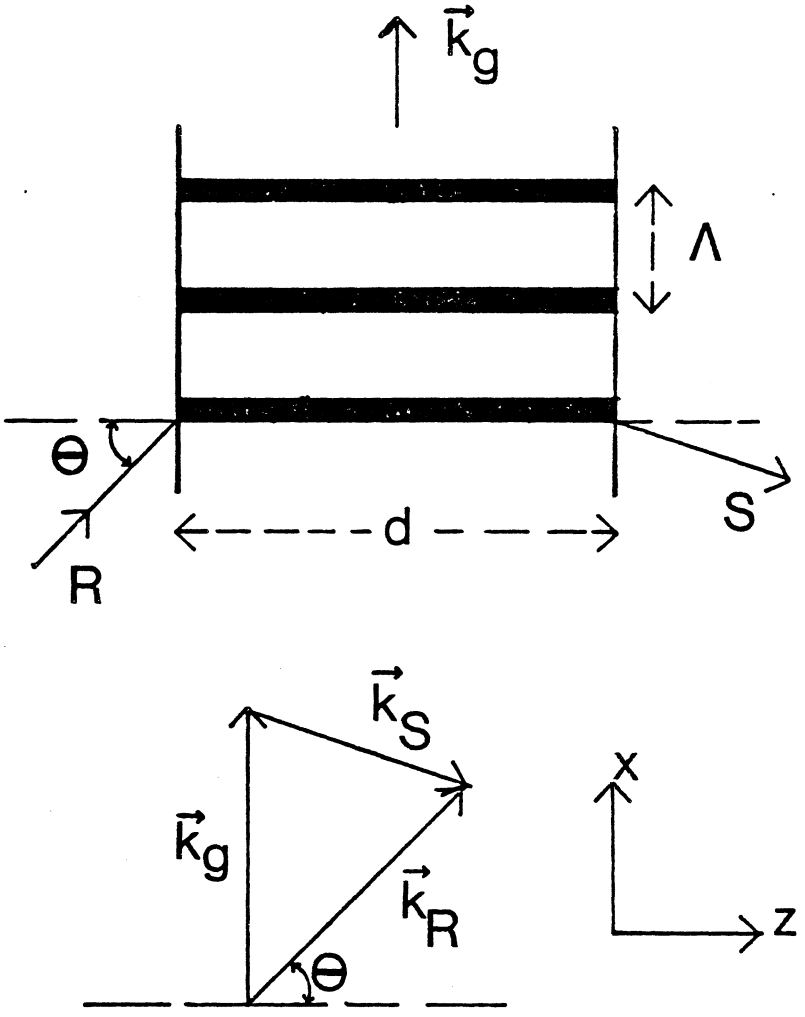

Figure 10. Coupled-wave model of thick gratings.

where $\vec{R}(z)$ and $\vec{S}(z)$ are, respectively, the amplitude vectors of the reference (incident) and signal waves, and $\vec{k}_R$ and $\vec{k}_S$ are the respective propagation vectors satisfying the (Bragg) condition shown in Figure 10.

$$\vec{k}_g = k_g \hat{x} = \vec{k}_R - \vec{k}_S \tag{20}$$

Here, $\vec{k}_g$ is the grating wavevector related to the grating period Λ by $k_g = 2\pi/\Lambda$. The plane wave equation satisfied by the electric field $\vec{E}$ in the grating medium is

$$\nabla^2 \vec{E} + \left(\frac{\omega^2}{c^2} \varepsilon - i\ \omega\mu\sigma\right)\vec{E} = 0 \tag{21}$$

Here ε, μ and σ are, respectively, the dielectric constant, the permeability, and the conductivity of the medium and are assumed to be independent of the y-direction.

The complex index of refraction of an optical medium can be written as

$$\tilde{n} = n_R + i\ n_I = n + i\ \frac{\lambda}{4\pi}\ \alpha \tag{22}$$

where n is the (conventional) real refractive index of the medium, and α is the absorption coefficient of the medium at the (free-space) wavelength λ. When the medium is exposed to light, both parts of $\tilde{n}$ change, and sinuosoidal spatial modulation is assumed, i.e.,

$$n = \bar{n} + \Delta n \cos (k_g x) \tag{23}$$

$$\alpha = \bar{\alpha} + \Delta\alpha \cos (k_g x) \tag{24}$$

with (practically)

$$\bar{\alpha},\ \Delta\alpha << \frac{2\pi}{\lambda}\,\bar{n} \quad \text{and} \quad \Delta n << \bar{n}$$

Here, $\bar{n}$ and $\bar{\alpha}$ are the average refractive index and absorption coefficient of the medium, respectively, and Δn and $\Delta\alpha$ are the respective spatial modulation amplitudes. If one defines a coupling constant between the reference and signal waves

$$\kappa = \frac{\pi}{\lambda}\,\Delta n \; - \; i\,\frac{\Delta\alpha}{2} \tag{25}$$

and if similar behavior to that in equations (23) and (24) is assumed for Δn and $\Delta\alpha$, then equation (21) can be written as

$$\nabla^2\vec{E} + (\beta^2 - 2i\bar{\alpha}\beta + 4\kappa\beta \cos k_g x)\,\vec{E} = 0 \tag{26}$$

where

$$\bar{\alpha} = \mu c\bar{\sigma}/2\,\sqrt{\bar{\varepsilon}}; \quad \beta = \frac{2\pi}{\lambda}\,\bar{n} = \frac{2\pi}{\lambda}\sqrt{\bar{\varepsilon}} \tag{27}$$

By substituting equations (19) and (20) in equation (26) one obtains the following coupled equations

$$\cos\theta\ \partial_z R + \bar{\alpha}R = -i\ \kappa\ S \tag{28}$$

$$\cos\theta\ \partial_z S + \bar{\alpha}S = -i\ \kappa\ R \tag{29}$$

where higher order diffraction terms and second derivatives were neglected.

The general solution of the above equations may be written as

$$R(z) = r_1 e^{\gamma_1 z} + r_2 e^{\gamma_2 z} \tag{30}$$

$$S(z) = s_1 e^{\gamma_1 z} + s_2 e^{\gamma_2 z} \tag{31}$$

γ_1 and γ_2 can be obtained by substituting equations (30) and (31) in the coupled equations (28) and (29):

$$\gamma_{1,2} = \frac{-\bar{\alpha}}{\cos\theta} \pm i \frac{\kappa}{\cos\theta} \tag{32}$$

For a transmission grating at z = d, the boundary conditions are

$$R(0) = 1, \quad S(0) = 0 \tag{33}$$

which give

$$r_1 + r_2 = 1, \quad s_1 + s_2 = 0 \tag{34}$$

Inserting equations (32) - (34) in equation (31), one obtains the amplitude of the signal wave to be

$$S = -i\, e^{\frac{-\bar{\alpha}d}{\cos\theta}} \sin\left(\frac{\kappa d}{\cos\theta}\right)$$

$$= \frac{1}{2} e^{\frac{-\bar{\alpha} d}{\cos\theta}} \left(e^{\frac{-i\kappa d}{\cos\theta}} - e^{\frac{i\kappa d}{\cos\theta}}\right) \tag{35}$$

The diffraction efficiency η, which is the fraction of the incident wave converted into signal wave is defined (assuming unit incident wave

amplitude) as (cf. equation (158) in reference 22).

$$\eta = S\ S^* \tag{36}$$

Hence, the diffraction efficiency in the case of a grating arising from the modulation in both the absorption coefficient and refractive index of the medium is given by [33]

$$\eta = e^{-2\bar{\alpha}\xi}\ [\sinh^2(\frac{\xi}{2}\ \Delta\alpha) + \sin^2(\frac{\pi\xi}{\lambda}\ \Delta n)] \tag{37}$$

where $\xi = d/\cos\theta$, and the exponential term insures that $\eta \leq 1$.

For normal incidence on the sample ($\theta = 0$), expression (37) for the diffraction (scattering) efficiency reduces to

$$\eta = e^{-2\bar{\alpha}d}\ [\sinh^2(\frac{d}{2}\ \Delta\alpha) + \sin^2(\frac{\pi d}{\lambda}\ \Delta n)] \tag{38}$$

Equation (38) is true for a simple two-level model [33]. Practically, $\eta < 10^{-2}$ (e.g., in this study, $\eta \sim 10^{-3}$) and hence, equation (38) can be approximated by

$$\eta = e^{-2\bar{\alpha}d}\ [(\frac{d}{2}\ \Delta\alpha)^2 + (\frac{\pi d}{\lambda}\ \Delta n)^2] \tag{39}$$

The scattering efficiency η is usually experimentally obtained. The quantities $\Delta\alpha$ and Δn are of interest because their values determine the type of grating constructed in the sample under study. The change in the index of refraction Δn is normally calculated from equation (38) whenever $\Delta\alpha$ is known. Measurements of Δn in ruby were reported, however [45,47]. In most of the published works to date, $\Delta\alpha$ is calculated

without considering the contribution from the Δn term. In attempt to characterize the gratings established in various experiments, two approaches are advanced: one by Fayer and his group [38] and the other by Hill [43]; these are instantly discussed below.

In a damped oscillator model, the real and imaginary parts of the complex index of refraction $\tilde{n}$ are related by [38]

$$n^2 - 1 = \sum_j \frac{N_j f_j' (\omega_j^2 - \omega^2)}{(\omega_j^2 - \omega^2)^2 + \gamma_j^2 \omega^2} = \sum_j n_j' \tag{40}$$

and

$$2n\alpha = \frac{4\pi}{\lambda} \sum_j \frac{N_j f_j' \gamma_j \omega}{(\omega_j^2 - \omega^2)^2 + \gamma_j^2 \omega^2} = \sum_j \alpha_j' \tag{41}$$

where $f_j' = \frac{4\pi e^2}{m} f_j$ with f_j being the oscillator strength of the jth transition, γ_j and ω_j are, respectively, the absorption linewidth and maximum (frequency), and N_j is the number density of ions in the initial state of the jth transition. n_j' and α_j' are the contributions of the absorption band to n and α, respectively.

For wavelengths tuned in the neighborhood of the absorption peak, i.e., $\omega \approx \omega_o$ where ω_o is the frequency at the peak of absorption, only one term in each of equations (40) and (41) is considered. Moreover, if for simplicity, one assumes no contributions arise from the close-by bands one can write (40) as [38]

$$\frac{d}{dx} (n^2 - 1) = \frac{d}{dx} n_o'$$

which leads to

$$\frac{dn}{dx} = \frac{d}{dx} \left\{ \frac{1}{2n_o} \frac{2N_o f'_o (\omega_o - \omega)}{\omega_o [4(\omega_o - \omega)^2 + \gamma_o^2]} \right\} \tag{42}$$

where x is any parameter representing strain or excited state concentration etc. Similarly, one can write the variation of α using equation (41) as

$$\frac{d\alpha}{dx} = \frac{d}{dx} \{\alpha_o (\omega) \}$$

$$= \frac{d}{dx} \left\{ \frac{4\pi}{\lambda} \frac{1}{2n_o} \frac{N_o f'_o \gamma_o}{\omega_o [4(\omega_o - \omega)^2 + \gamma_o^2]} \right\} \tag{43}$$

where $\omega_o^2 - \omega^2 = (\omega_o+\omega)(\omega_o-\omega) \simeq 2\omega_o (\omega_o-\omega)$ was used in obtaining the above equations. Moreover, a term depending on $(\frac{dn}{dx})$ in equation (43) was omitted because it is very small $(\frac{dn}{dx} << 1)$

If the sample has N_o ions per unit volume when unperturbed and N_{2p} ions per unit volume in the excited states at the grating peaks, then the grating peak-null variation is given by

$$2\Delta n_{ex} (\omega; N_{2p}) = \frac{dn}{dN_o} \Delta N_o$$

$$= -(\frac{N_{2p}}{N_o})(\frac{\lambda}{2\pi})(\frac{\omega_o - \omega}{\gamma_o}) \alpha_o(\omega) \tag{44}$$

where $\alpha_o(\omega)$ is defined in equation (43). Similarly, from equation (43) one has

$$2\,\Delta\alpha_{ex}\,(\omega;\ N_{2p}) = \frac{d\alpha}{dN_o}\,\Delta N_o$$

$$= -\frac{N_{2p}}{N_o}\,\alpha_o(\omega) \tag{45}$$

The subscript "ex" stands for excited-state contribution. Substituting (44) and (45) in (39), the excited-state diffraction efficiency reduces to

$$\eta_{ex} = \left(\frac{N_{2p}}{N_o}\frac{d}{4}\right)^2 e^{-2\bar{\alpha}d}\left[1 + \left(\frac{\omega_o - \omega}{\gamma_o}\right)^2\right]\alpha_o^2(\omega) \tag{46}$$

Equation (46) is true within the limitations of the assumptions made in this approach, otherwise one must go back to equation (38) or (39).

On the other hand, Hill forwarded a simple two-level model [43] workable for ruby (and alexandrite) having the absorption coefficient of the sample at an excitation wavelength λ given by

$$\alpha(\lambda) = \sigma_1(\lambda)N_o + [\sigma_2(\lambda) - \sigma_1(\lambda)]N_2 \tag{47}$$

where $N_o = N_1 + N_2$ is the total concentration of active ions in the sample, with N_1 and N_2 being the concentrations of ions in the ground and excited states, respectively, and $\sigma_1(\lambda)$ and $\sigma_2(\lambda)$ are the ground and excited state absorption cross sections at the excitation wavelength λ, respectively. One solves the rate equations of this system for steady-state situation and obtains for a pumping intensity $I(\lambda)$

$$N_2 = \frac{N_o\,\sigma_1(\lambda)\,I(\lambda)}{\sigma_1(\lambda)I(\lambda) + hc/\lambda\,\tau_{21}} \tag{48}$$

Here τ_{21} is the fluorescence decay time of level 2 to level 1. By substituting equation (48) in (47), the absorption coefficient comes out as

$$\alpha(\lambda) = N_o \sigma_1(\lambda) \left\{1 + \frac{[\sigma_2(\lambda) - \sigma_1(\lambda)]\, I(\lambda)}{\sigma_1(\lambda) I(\lambda) + hc/\lambda\, \tau_{21}}\right\} \tag{49}$$

Assuming a sinusoidal variation, with period Λ, of the intensity or energy density $I(\lambda)$ of the form

$$I(\lambda) = I_o \left(1 + \sin \frac{2\pi}{\Lambda} \hat{k}.\vec{r}\right)$$

one obtains for the modulation of the absorption coefficient, i.e., the difference in absorption coefficient values at the peak (α_p) and valley (α_v) of the interference pattern, the following expression

$$2\Delta\alpha = \alpha_p - \alpha_v = (\sigma_2 - \sigma_1)\, N_{2p}$$

$$= \frac{2I_o\, N_o\, \sigma_1\, (\sigma_2 - \sigma_1)}{2I_o\, \sigma_1 + hc/\lambda\, \tau_{21}} \tag{50}$$

The expression for Δn is not predicted by this simple two-level model. Furthermore, the above treatment was dedicated for excited-state gratings only.

However, thermal gratings [34] could arise upon optically exciting a medium; ultrasonic waves are generated in the medium [35-40]. They can be easily distinguished from excited-state gratings because of their distinct faster decay times and moreover, the extrapolation of their

decay rates to zero when varied with the pump beam crossing angle θ in four-wave mixing experiments. On the time scale of our experiments on alexandrite, FWM signals arising from thermal gratings were not observed. Nevertheless, it is worthwhile, in the context of FWM techniques to supply information about the generation (and detection) of such gratings. A detailed exposition of this is presented in the Appendix.

C. Experimental

The sample investigated was an oriented cube of $BeAl_2O_4$, known as chrysoberyl, with each edge measuring about 5 mm. It contained 0.0897 at % Cr^{3+} ions with about 78% of these being in mirror sites and the rest in inversion sites. Figure 11 shows the structure of chrysoberyl projected on the orthorhombic c-axis [41]. The energy level diagram of Cr^{3+} ions in chrysoberyl is given in Figure 12 [24].

The experimental setup for degenerate four-wave mixing (FWM) measurements is illustrated in Figure 13. Similar configurations were adopted for energy migration studies [20,22]. In this study, an argon ion laser or a ring dye laser (pumped by the former) was used a source of excitation. A Reference Interference System, referred to by "Stabilok" in Figure 13, was included to insure the stability in wavelength of the dye laser output. The main laser beam is variably split (VBS) into two parts: two pumping beams P_1 and P_2 interfering in the sample and a probe beam P_r, all of which are aligned and focused into the sample by a set of mirrors (M) and lenses (L). The probe beam P_r counterpropagates (conjugately) pump beam P_1 and the FWM signal

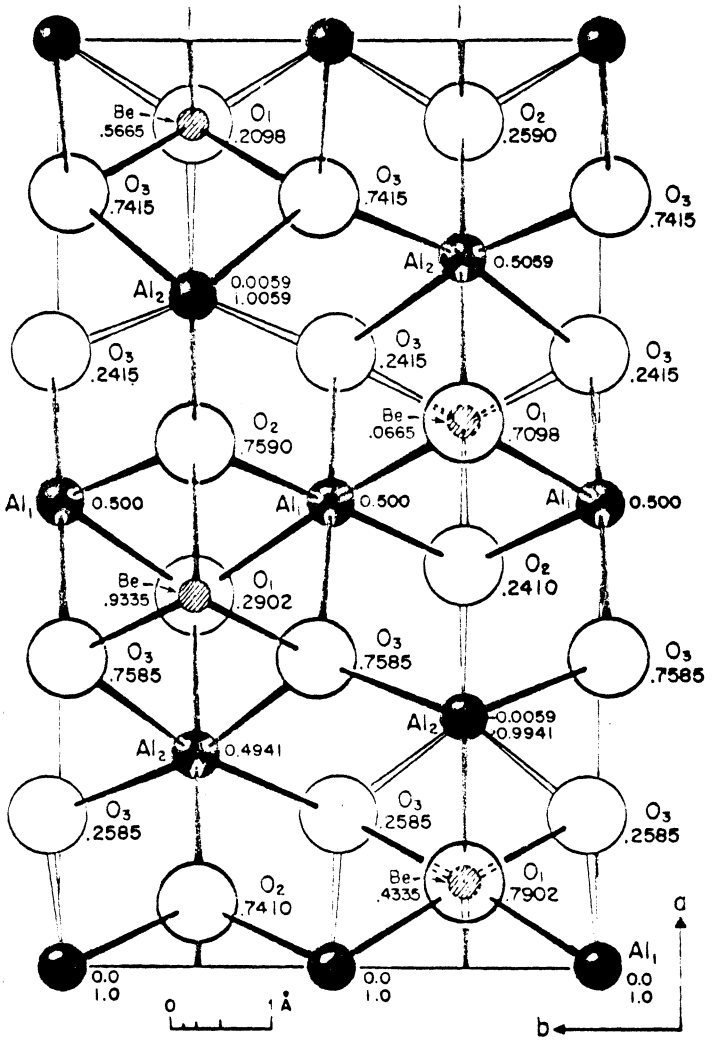

Figure 11. Structure of $BeAl_2O_4$ projected along its c-axis. The numbers correspond to heights of atoms in cell fractions [41].

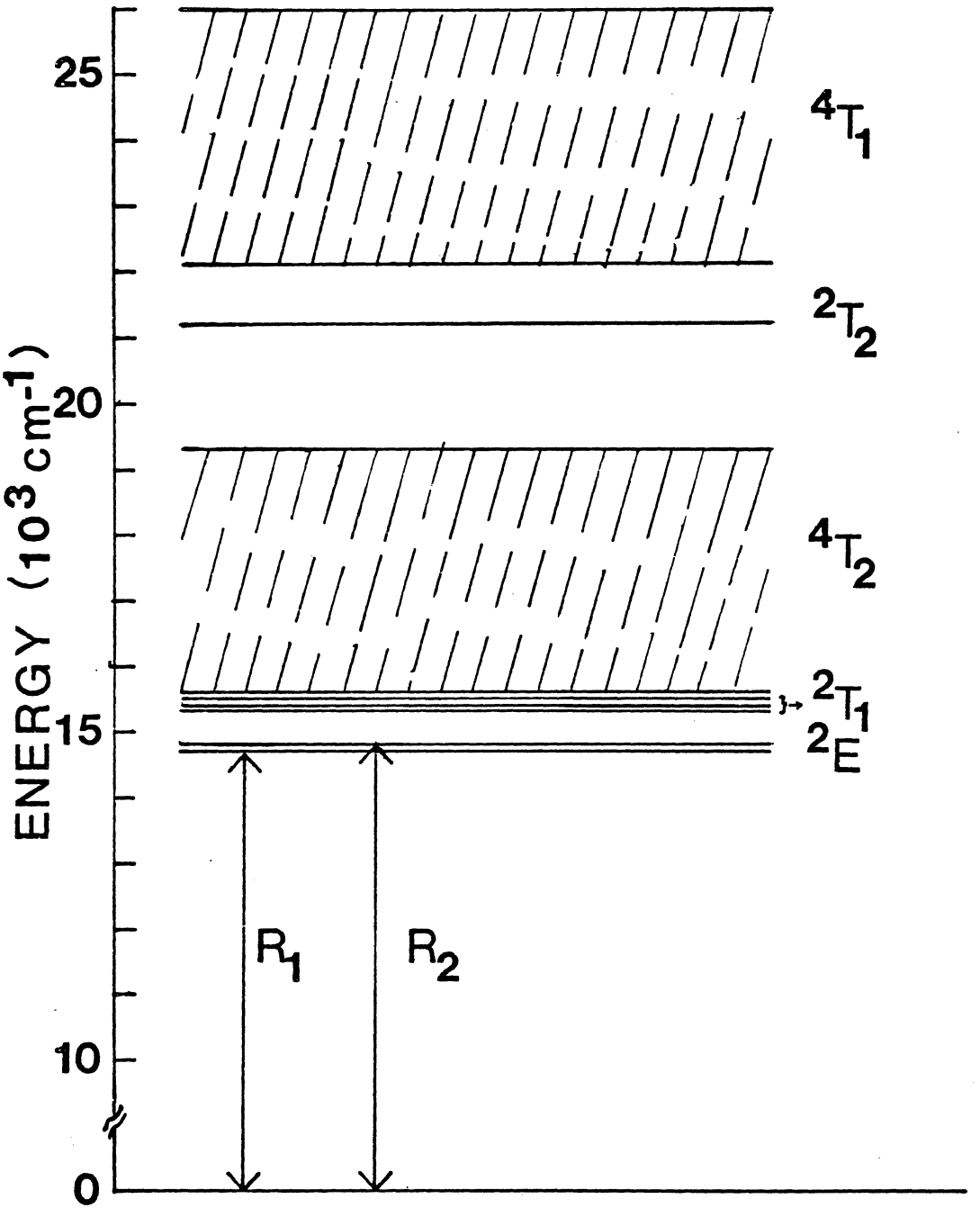

Figure 12. Energy level diagram of Cr^{3+} in alexandrite crystal.

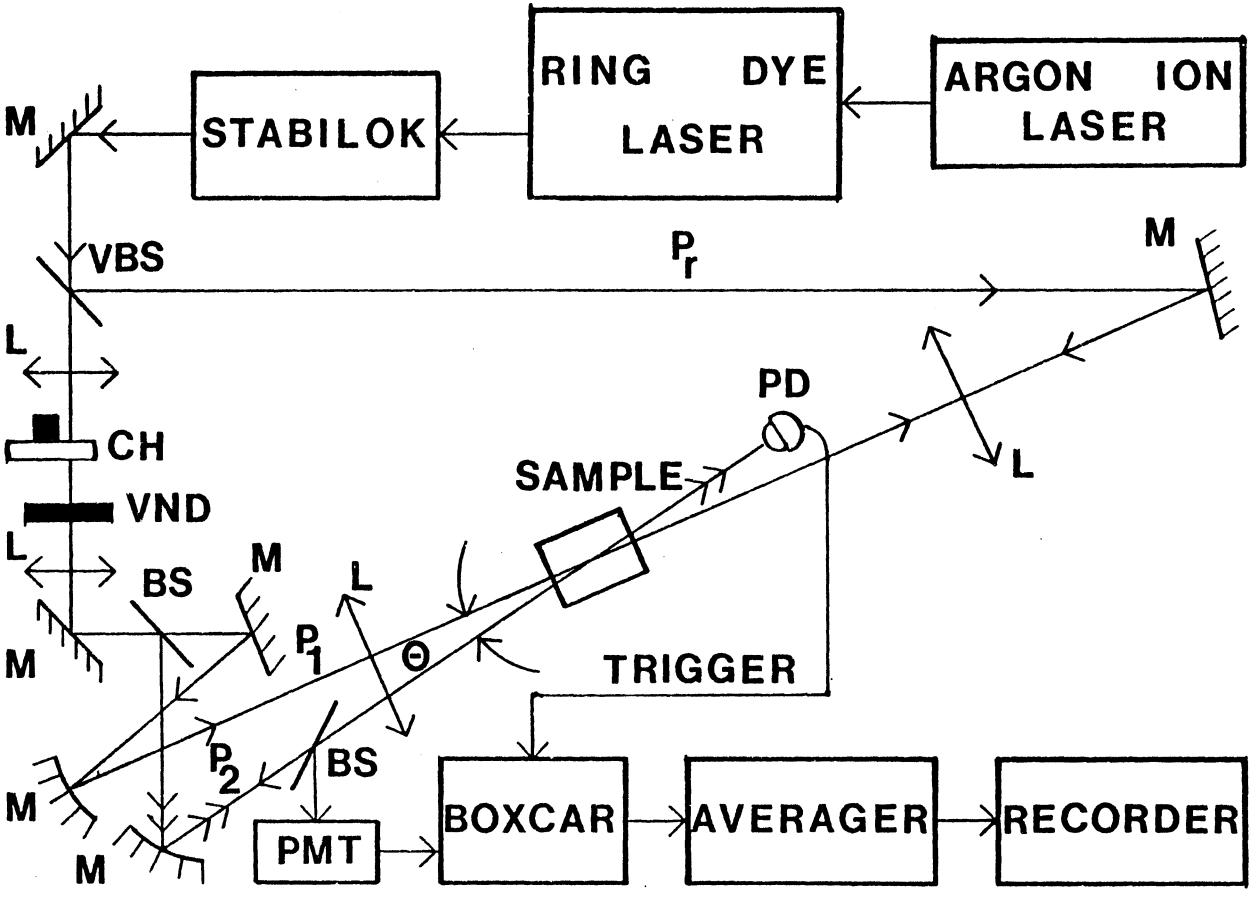

Figure 13. Four-Wave Mixing experimental configuration.

propagates in the direction conjugate to pump beam P_2. A beam splitter (BS) drives the signal into a photomultiplier whose output is processed by a signal averager made by PAR. The contents of the averager are then displayed on a chart recorder. A variable neutral density filter (VND) is utilized to control the pumping powers and a chopper (CH) is included for lifetime measurements. In contrast, the beams are not chopped during scattering efficiency measurements and moreover, a lock-in amplifier is implemented to give a measure of the intensity of the FWM signal. All measurements (of this chapter) were taken at room temperature.

Attempts were made to perform the experiments with all combinations of crystal orientations and laser polarizations. However, strong FWM signals were only observed with the laser beams polarized parallel to the b-axis with propagation occuring along either of the other two crystallographic directions as shown in Figure 14. The absorption spectra were taken on a Cary 14 spectrophotometer for various crystal orientations and are shown in Figure 15-A. To obtain the vertical scale in units of cm^{-1}, i.e., that of the absorption coefficient, one should divide by the thickness of the sample in cm. On the other hand, emission spectra were taken using a 1-m Czerny-Turner monochromator and are depicted in Figure 15-B.

D. Data and Interpretation

In investigating the four-wave mixing signal in alexandrite, three excitation wavelengths were employed: 488.0 nm, 514.5 nm (argon ion laser), and 579.1 nm (ring dye laser). With the excitation of the shorter wavelengths and in the bulk of the sample, measurements of the

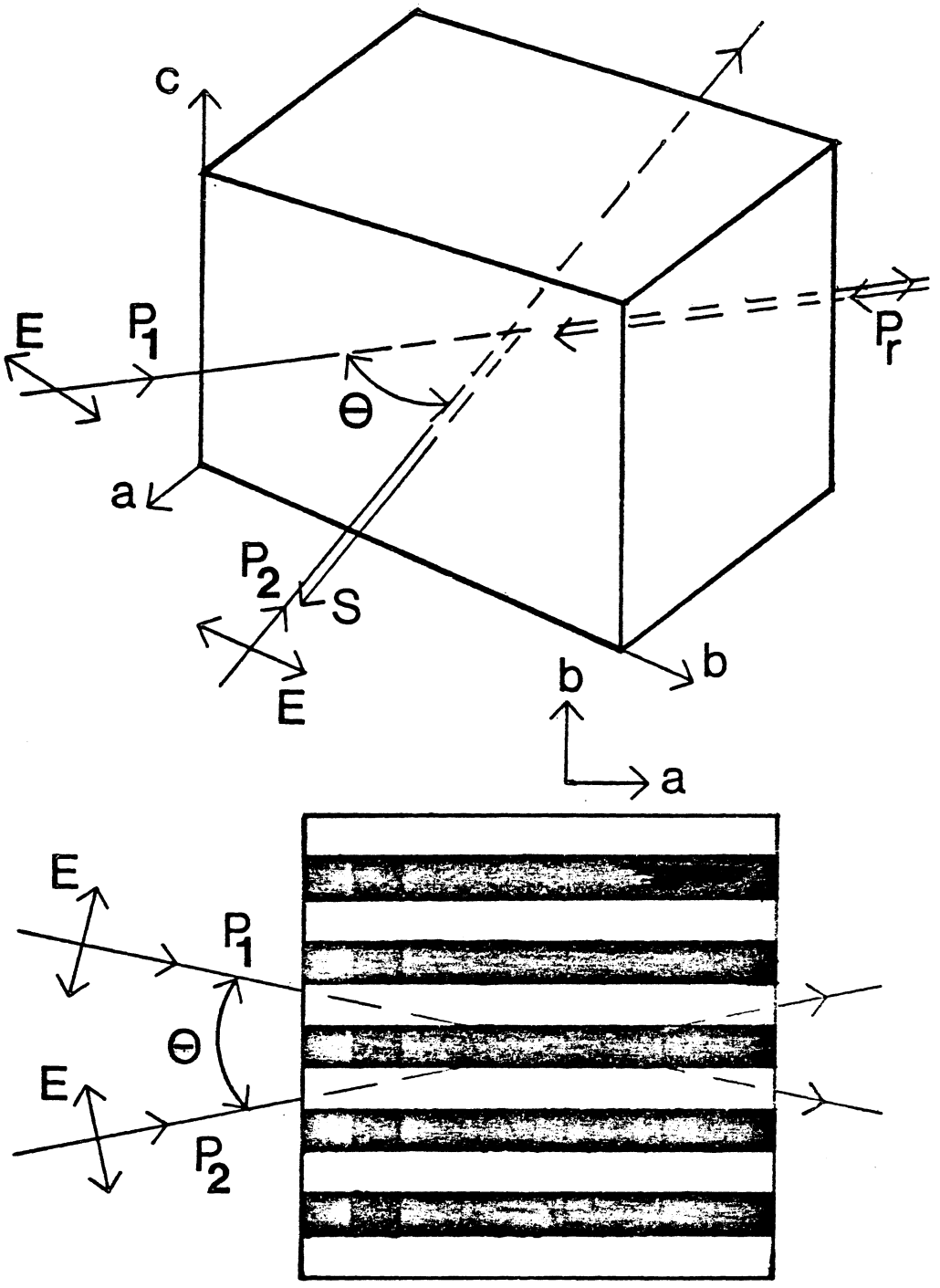

Figure 14. FWM signal detected with pump beams polarized parallel to the b-axis of alexandrite.

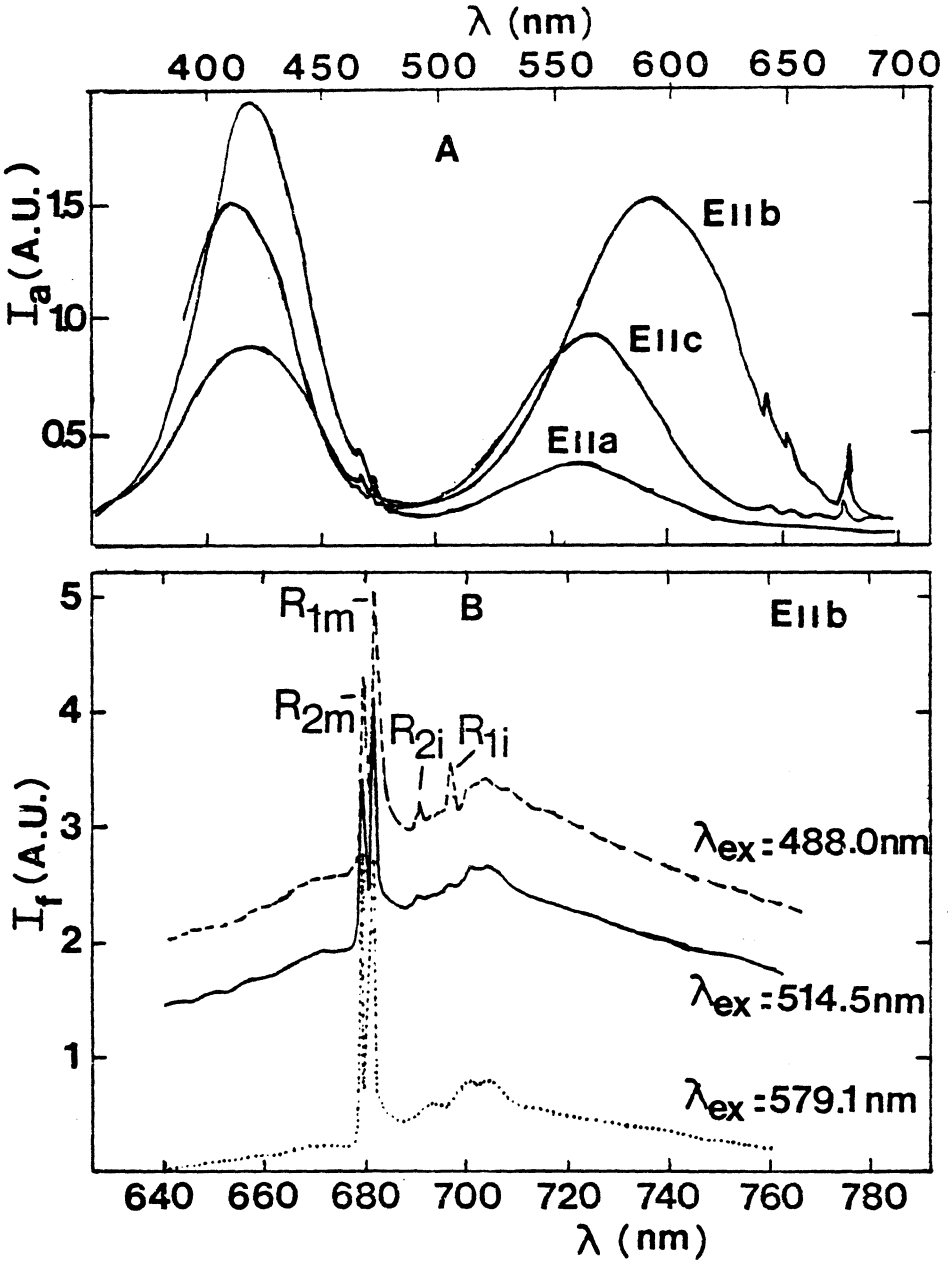

Figure 15. (A) Absorption spectra of $BeAl_2O_4:Cr^{3+}$ for different polarization directions. (B) Fluorescence spectra of $BeAl_2O_4:Cr^{3+}$ with laser excitation polarized E // b .

variation of the signal decay rate with pump power were taken for the pump beam crossing angle θ with the values 1.75°, 6°, 7.2°, and 26.5°. Figure 16-B shows this variation and Tables V and VI list the corresponding data. With the long wavelength excitation, the variation of the signal decay rate with pump power was measured for θ = 3.5°, 6°, 11.5°, 17.3°, and 25°; the corresponding data are given in Table VII. Moreover, decay rate variation with the crossing angle θ of the pump beams was measured, as shown in Figure 16-A, for all of the excitation wavelengths mentioned above. These measurements are listed in Table VIII. On the other hand, surface measurements of the variation of the signal decay rate with pump power are listed in Tables IX and X, and are shown in Figure 17.

In order to study the variation of the scattering efficiency of alexandrite with pump power, the relative fraction of the probe beam converted to the signal beam, η was measured for various pump powers and beam crossing angles θ. Figure 18 shows the variation of η with the product of the powers of the two pump beams, for the excitation wavelengths 488.0 nm and 514.5 nm for θ = 6° and 26.5° in the bulk of the sample (the upper two plots); also shown in the lower part of the figure the data with θ = 26.5° at the surface of the sample, however. Data taken for other values of θ show the same pattern of Figure 18 and hence are not exhibited there. The respective data for η variation with pump beam powers for various crossing angles and excitation wavelengths for both bulk and surface measurements are given in Tables XI - XII. The values of η are normalized to the maximum value of each set of measurements.

Figures 16 and 18 summarize the observed FWM characteristics in the

TABLE V

GRATING DECAY RATE AS A FUNCTION OF PUMP POWER FOR λ_{ex} = 488.0 nm IN THE BULK OF THE SAMPLE

θ = 1.75°		θ = 6°	
I (mW)	K(s^{-1})	I (mW)	K(s^{-1})
100.5	21.58	111.3	44.64
188.8	26.43	213.1	46.93
230.8	56.53	266.5	54.44
289.4	40.77	335.0	52.66
349.4	34.93	378.9	47.89
438.9	32.05	467.7	50.05
505.0	51.31	592.0	40.24

θ = 7.2°		θ = 26.5°	
I (mW)	K(s^{-1})	I (mW)	K(s^{-1})
115.5	44.74	122.6	44.07
222.7	46.51	232.8	45.11
278.4	47.08	283.8	43.96
348.1	45.89	354.8	45.29
397.6	46.19	427.2	45.35
492.2	46.30	537.4	44.94
600.0	45.68	620.0	45.87

TABLE VI

GRATING DECAY RATE AS A FUNCTION OF PUMP POWER FOR λ_{ex} = 514.5 nm IN THE BULK OF THE SAMPLE

θ = 1.75°		θ = 6°	
I (mW)	K(s^{-1})	I (mW)	K(s^{-1})
120.5	45.05	163.7	50.51
154.0	45.13	221.5	52.85
208.1	38.85	288.4	52.71
255.5	43.69	326.8	52.69
311.0	46.17	415.5	56.18
365.0	41.72	515.0	50.61

θ = 7.2°		θ = 26.5°	
I (mW)	K(s^{-1})	I (mW)	K(s^{-1})
73.0	42.44	67.0	41.51
144.7	47.98	132.0	43.94
196.1	47.35	170.0	44.40
255.4	45.15	228.0	43.22
289.8	45.35	280.0	43.63
368.6	45.02	340.0	44.21
415.0	44.94	395.0	44.60

Table VII

GRATING DECAY RATE (s^{-1}) AS A FUNCTION OF PUMP POWER FOR λ_{ex} = 579.1 nm IN THE BULK OF THE SAMPLE

$I_{\theta(°)}$ (mW)	3.5	6	11.5	17.3	25
21.9	5618	5376	6211	4000	5240
63.6	5988	6024	6173	4160	6720
137.0	6452	6211	5263	5720	7400

TABLE VIII

GRATING DECAY RATE VERSUS CROSSING ANGLE IN THE BULK OF THE SAMPLE

λ_{ex} = 488.0 nm		λ_{ex} = 514.5 nm		λ_{ex} = 579.1 nm	
θ(°)	K(s^{-1})	θ(°)	K(s^{-1})	θ(°)	K(s^{-1})
0.0	20.35	0.0	19.89	0.0	3333
1.75	37.66	1.75	43.44	3.5	6019
6.00	48.12	6.00	52.59	6.0	5870
7.20	46.06	7.20	45.46	11.5	5882
26.50	44.94	26.50	43.64	17.3	4627
				25.0	6453

TABLE IX

GRATING DECAY RATE AS A FUNCTION OF PUMP POWER FOR λ_{ex} = 488.0 nm AT THE SURFACE OF THE SAMPLE

θ = 7.2°		θ = 26.5°	
I (mW)	K(s^{-1})	I (mW)	K(s^{-1})
115.5	51.57	114.3	42.99
222.7	37.33	215.1	51.65
278.4	43.92	266.4	42.64
348.1	41.58	341.1	43.40
397.6	49.36	408.2	44.25
492.2	43.37	532.3	41.20
600.0	42.66	544.5	39.81

TABLE X.

GRATING DECAY RATE AS A FUNCTION OF PUMP POWER FOR λ_{ex} = 514.5 nm AT THE SURFACE OF THE SAMPLE

θ = 7.2°		θ = 26.5°	
I (mW)	K(s^{-1})	I (mW)	K(s^{-1})
75.6	41.88	135.0	49.55
149.9	43.94	178.0	43.38
203.2	45.54	224.0	45.64
264.7	45.64	279.0	42.75
300.3	45.45	347.0	47.21
382.0	44.76	400.0	42.86
430.0	43.35		

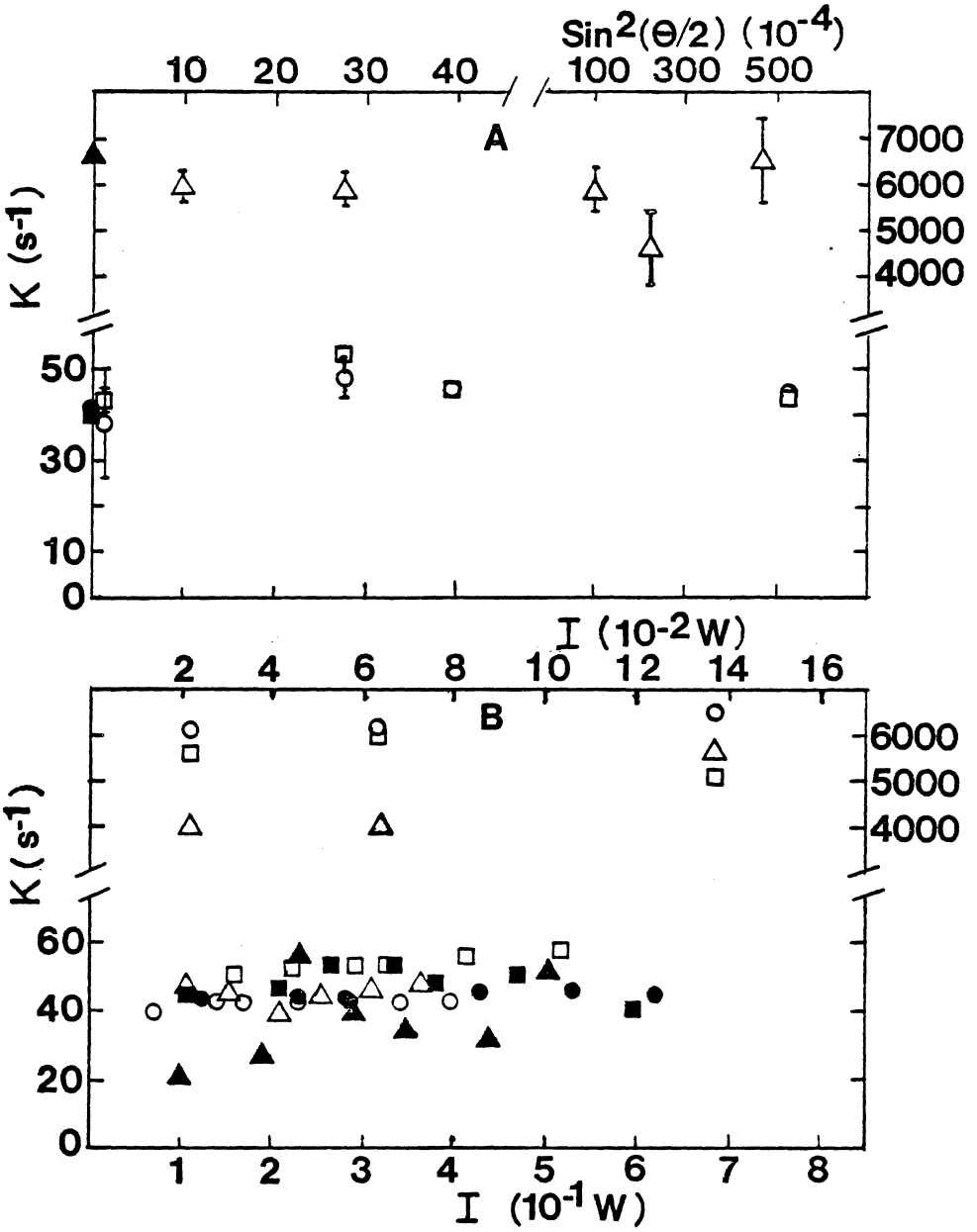

Figure 16. (A) FWM signal decay rate versus pump beam crossing angle θ: λ_{ex} = 488.0 nm (○); λ_{ex} = 514.5 nm (□); λ_{ex} = 579.1 nm (△); the solid points represent twice the fluorescence decay rates. (B) FWM signal decay rate versus pump beam power. Upper scale for λ_{ex} = 579.1 nm: θ=3.5° (○); θ=11.5° (△); θ=17.3° (□). Lower scale for λ_{ex}=488.0 nm: θ=1.75° (▲); θ=6.0° (■); θ=26.5° (●); and for λ_{ex}=514.5 nm: θ=1.75° (△); θ=6.0° (□); θ=26.5° (○).

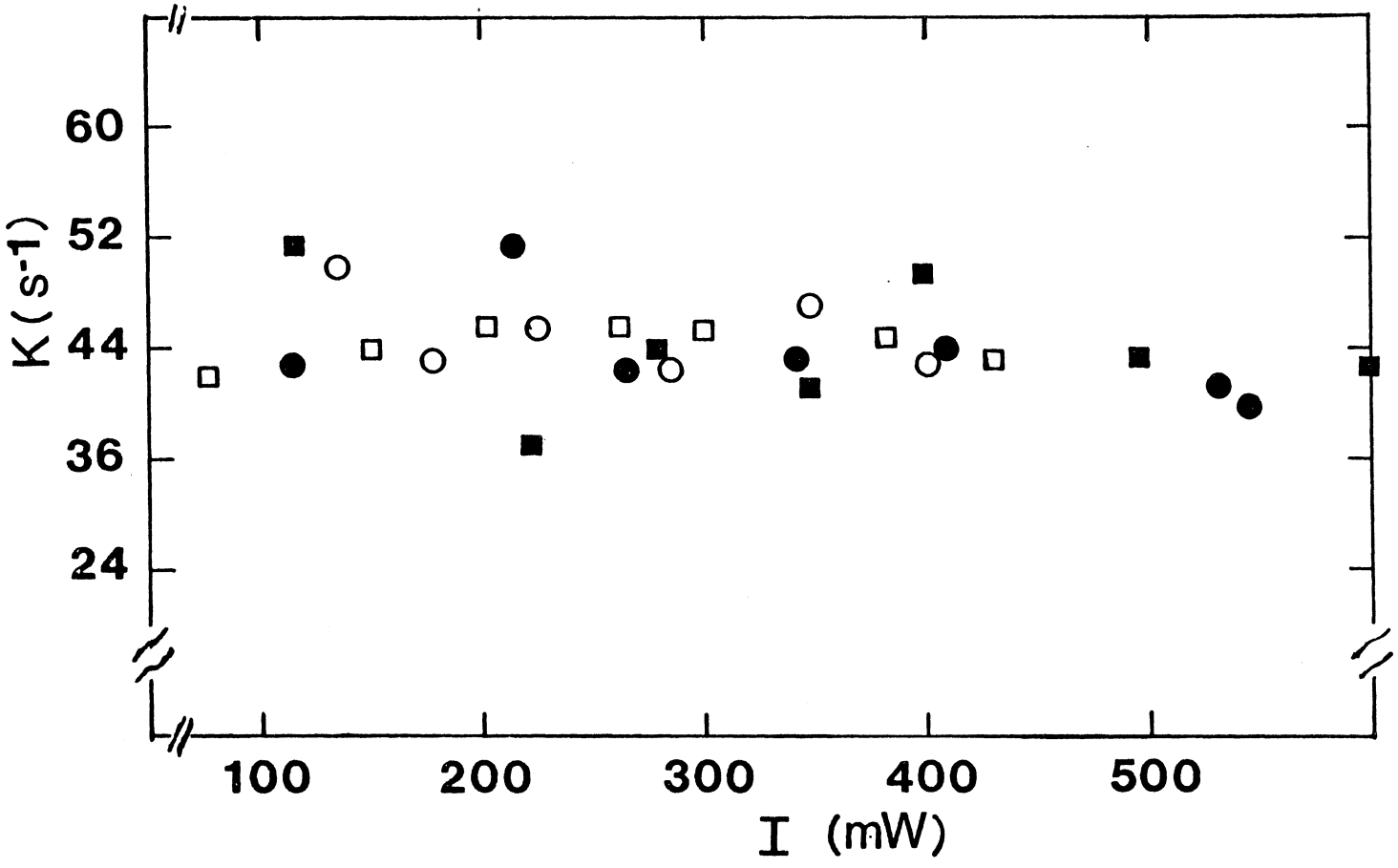

Figure 17. FWM signal decay rate versus pump beam power at the surface of the sample: λ_{ex} = 488.0 nm, θ = 7.2° (■); λ_{ex} = 488.0 nm, θ=26.5° (●); λ_{ex} = 514.5 nm, θ=7.2° (□); λ_{ex} = 514.5 nm, θ=26.5° (○).

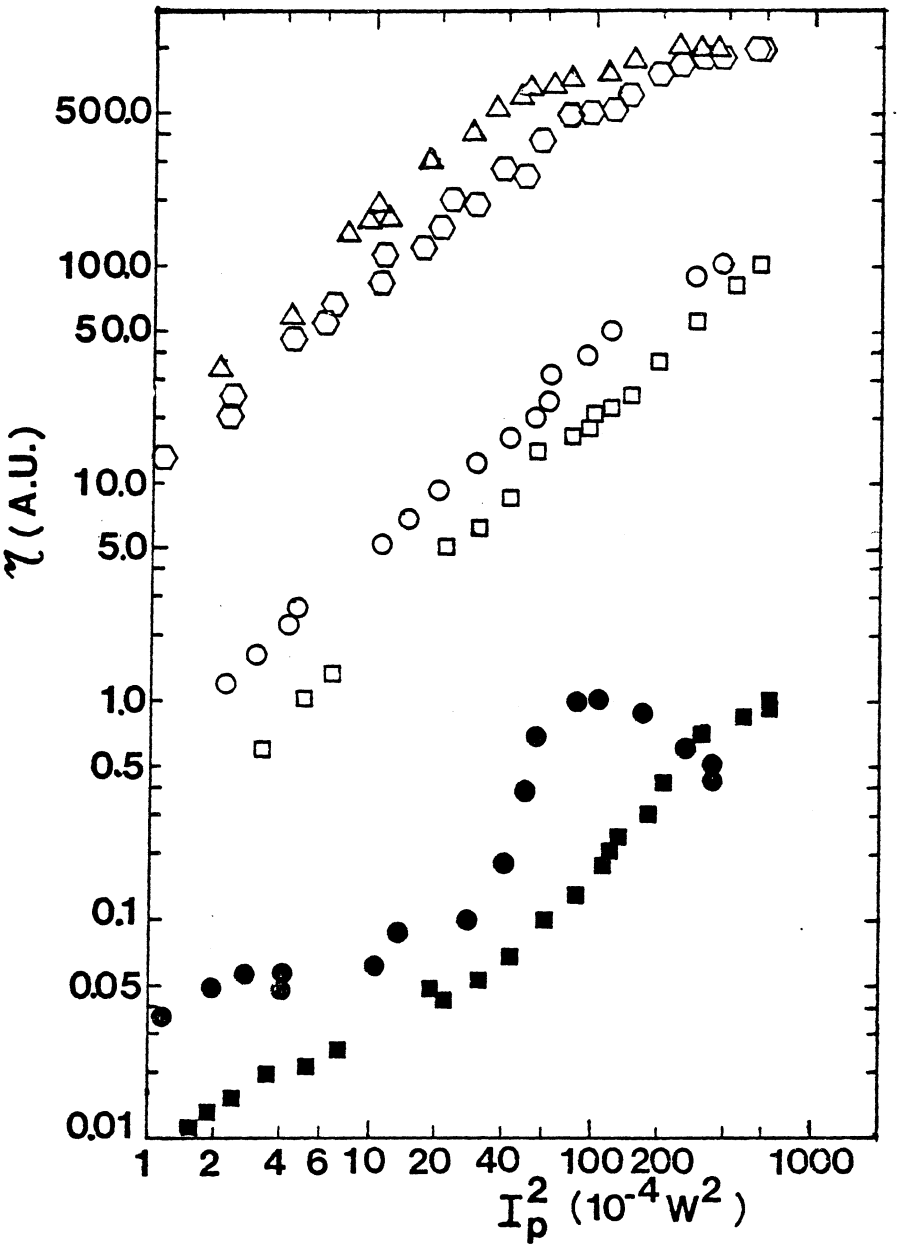

Figure 18. Fraction of probe beam converted to FWM signal beam as a function of the product of the powers of the laser pump beams. Bulk excitation: λ_{ex} = 488.0 nm, θ=6.0° (⬡); λ_{ex} = 514.5 nm, θ = 6.0° (△); λ_{ex} = 488.0 nm, θ=26.5° (□); λ_{ex} = 514.5 nm, θ=26.5° (○). Surface excitation: λ_{ex} = 483.0 nm, θ=26.5° (■); λ_{ex} = 514.5 nm, θ=26.5° (●).

TABLE XI

SCATTERING EFFICIENCY AS A FUNCTION OF THE PRODUCT OF THE PUMP BEAM POWERS IN THE BULK OF THE SAMPLE

$I_p^2(W^2)\times10^{-4}$	η(A.U.)	$I_p^2(W^2)\times10^{-4}$	η(A.U.)
λ_{ex} = 488.0nm, θ = 1.75°		λ_{ex} = 514.5nm, θ = 1.75°	
94.20	0.19	7.75	0.05
113.20	0.23	8.74	0.04
121.00	0.19	11.90	0.06
141.70	0.23	16.90	0.07
172.00	0.29	17.75	0.06
228.00	0.37	23.75	0.08
337.30	0.46	24.30	0.10
526.30	0.69	27.75	0.10
688.00	1.00	33.80	0.13
		44.30	0.15
		50.80	0.16
		52.40	0.21
		76.60	0.26
		101.60	0.30
		155.00	0.45
		231.50	0.68
		288.40	0.91
		307.80	0.96
		314.00	1.00
λ_{ex} = 488.0nm, θ = 6°		λ_{ex} = 514.5nm, θ = 6°	
1.12	0.01	2.00	0.03
2.20	0.02	4.31	0.06
2.30	0.03	7.33	0.14
4.24	0.05	9.20	0.16
5.94	0.06	10.40	0.19
6.40	0.07	11.67	0.16
10.40	0.08	17.40	0.30
10.75	0.11	28.20	0.41
16.75	0.12	35.70	0.53
20.00	0.15	46.70	0.60
22.22	0.20	50.60	0.55
28.75	0.19	66.60	0.56
38.00	0.28	77.80	0.61
48.75	0.26	113.90	0.75
58.00	0.38	147.40	0.86
75.70	0.49	239.00	1.00

TABLE XI (Continued)

$I_p^2(W^2)\times10^{-4}$	η(A.U.)	$I_p^2(W^2)\times10^{-4}$	η(A.U.)
λ_{ex} = 488.0nm, θ = 6°		λ_{ex} = 514.5nm, θ = 6°	
93.50	0.51	298.10	0.96
95.80	0.50	360.00	0.95
118.40	0.52		
143.10	0.61		
183.30	0.76		
243.20	0.83		
373.90	0.91		
505.20	0.99		
549.70	1.00		
584.20	0.99		
λ_{ex} = 488.0nm, θ = 7.2°		λ_{ex} = 514.5nm, θ = 7.2°	
0.04	0.008	0.11	0.048
0.08	0.014	0.15	0.062
0.09	0.018	0.21	0.083
0.13	0.025	0.30	0.103
0.14	0.028	0.43	0.138
0.20	0.050	0.56	0.159
0.21	0.036	0.62	0.179
0.29	0.056	0.65	0.193
0.36	0.056	0.96	0.241
0.38	0.069	1.27	0.448
0.54	0.097	1.91	0.586
0.55	0.100	2.89	1.000
0.73	0.128	3.59	0.966
0.81	0.150	3.84	0.900
0.83	0.167	3.91	0.862
1.04	0.161		
1.24	0.167		
1.33	0.183		
1.56	0.239		
1.89	0.261		
2.51	0.372		
3.71	0.500		
7.57	1.000		

TABLE XI (Continued)

$I_p^2(W^2)\times10^{-4}$	η(A.U.)	$I_p^2(W^2)\times10^{-4}$	η(A.U.)
λ_{ex} = 4.88.0nm, θ = 26.5°		λ_{ex} = 514.5nm, θ = 26.5°	
3.23	0.006	2.20	0.012
4.92	0.010	2.88	0.016
6.58	0.013	4.07	0.022
21.50	0.050	4.48	0.027
29.00	0.064	10.76	0.051
40.80	0.086	14.56	0.067
54.60	0.137	20.16	0.089
77.55	0.164	29.00	0.124
93.60	0.182	40.95	0.164
101.75	0.205	54.00	0.196
116.00	0.227	60.63	0.244
143.00	0.250	63.55	0.311
187.50	0.364	92.22	0.383
282.00	0.546	123.83	0.500
437.00	0.818	282.00	0.889
572.00	1.000	372.00	1.000
λ_{ex} = 579.1nm, θ = 11.5°			
1.20		0.043	
1.29		0.052	
1.30		0.048	
2.10		0.062	
2.20		0.071	
2.80		0.071	
3.60		0.081	
4.50		0.129	
5.90		0.167	
6.40		0.152	
8.40		0.224	
9.90		0.238	
14.30		0.405	
18.70		0.524	
30.30		0.714	
39.00		0.952	
37.80		1.000	
40.30		0.905	
45.60		0.952	

TABLE XII

SCATTERING EFFICIENCY AS A FUNCTION OF THE PRODUCT OF THE PUMP BEAM POWERS AT THE SURFACE OF THE SAMPLE

$I_p^2(W^2)\times10^{-4}$	η(A.U.)	$I_p^2(W^2)\times10^{-4}$	η(A.U.)
λ_{ex} = 488.0nm, θ = 7.2°		λ_{ex} = 514.5nm, θ = 7.2°	
0.28	0.086	0.12	0.045
0.31	0.086	0.14	0.065
0.53	0.137	0.23	0.085
0.82	0.171	0.38	0.110
1.05	0.171	0.48	0.130
1.31	0.171	0.63	0.130
1.35	0.314	0.68	0.090
1.66	0.429	0.89	0.100
1.98	0.486	1.05	0.140
2.46	0.514	1.54	0.270
3.38	0.514	2.02	0.480
5.22	0.800	3.19	0.750
7.06	0.857	4.14	0.900
7.67	0.886	4.22	0.980
7.43	0.800	4.33	0.960
8.14	1.000	4.83	1.000
7.67	0.943	4.00	1.000
λ_{ex} = 488.0nm, θ = 26.5°		λ_{ex} = 514.5nm, θ = 26.5°	
1.58	0.011	1.15	0.036
1.90	0.013	1.88	0.048
2.38	0.015	2.70	0.056
3.45	0.019	3.94	0.048
5.16	0.021	10.44	0.060
7.14	0.024	13.00	0.085
7.40	0.026	19.00	0.050
22.50	0.042	26.68	0.100
31.50	0.052	38.50	0.180
43.20	0.067	48.75	0.380
62.35	0.100	55.35	0.680
85.00	0.133	82.50	1.000
108.30	0.178	106.20	1.000
118.00	0.207	164.25	0.840
130.20	0.244	255.75	0.600
178.50	0.304	336.00	0.500
213.30	0.422	336.00	0.440
307.20	0.700		
483.00	0.852		
644.00	0.963		
644.00	1.000		

bulk of the alexandrite sample. The signal decay was purely exponential for all measurements and the decay rate was found to be independent of pump beam crossing angle and of pump power. The magnitude of the decay rate was significantly different for long wavelength pumping compared to pumping with the two shorter wavelengths. For long wavelength dye laser pumping, the relative fraction of the probe beam converted to the signal beam varied quadratically with laser power. Pumping with the higher power argon ion laser at shorter wavelengths also produced quadratic dependences of FWM signal efficiencies at high pump beam crossing angles, but saturation effects were observed for small crossing angles. If the pumping beams are oriented to cross near the surface of the sample, a significant deviation from quadratic behavior and saturation effects is observed.

These results can be interpreted in terms of the model of FWM [33,42] based on scattering from a laser induced, transient population grating. The interference of the Gaussian wavefronts of the pump beams in the region of their crossing forms a sinusoidal pattern. This results in a similar spatial distribution of Cr^{3+} ions in the excited state. Because of the difference in the absolute value of the complex dielectric constant of the material when the Cr^{3+} ions are in the ground or excited states, this sinusoidal excited state population distribution acts as a diffraction grating which scatters the probe beam. When the Bragg condition is satisfied, this becomes the FWM signal beam. For no migration of the excited state energy and no thermal grating contribution, the scattered signal is theoretically predicted to decay exponentially with a decay rate equal to twice the fluorescence decay rate and independently of pump beam power and crossing angle. The solid

points in Figure 15-A for zero crossing angle represent twice the independently measured fluorescence decay rates. This shows agreement between theory and experiment for both types of laser excitation. The fact that the decay rates are significantly different for the two different types of laser excitation can be understood from the absorption and fluorescence spectra shown in Figure 15. The dye laser excitation at 579.1 nm efficiently excites Cr^{3+} ions in the mirror sites as demonstrated by the dominance of the two R_m lines in the fluorescence spectrum. The measured fluorescence decay rate is consistent with that of the coupled emission from the ^2E and $^4T_2$ levels of Cr^{3+} ions in this type of site [24]. On the other hand, the 488.0 and 514.5 nm excitation wavelengths of the argon laser excite Cr^{3+} ions in the inversion sites as seen by the enhancement of the R_i lines from these sites in the fluorescence spectrum. The smaller fluorescence decay rate is consistent with the weaker transition strengths of ions in this type of site [24].

The strength of the FWM signal depends on the difference of the concentration of ions in the excited state between the peak and valley regions of the grating and the modulation in the complex dielectric constant of the material when the ions are in the excited state and when they are in the ground state. The greater absorption strength for the E // b direction contributes to that fact the FWM signal is only strongly observed with this orientation, since the peak-to-valley excited state concentration difference will be maximum.

The complex dielectric constant and refractive index are related by

$$\sqrt{\tilde{\varepsilon}} = \sqrt{\varepsilon_R + i\,\varepsilon_I}$$

$$= n_R + i\, n_I$$

$$= n + i\,(\frac{\lambda}{4\pi})\ \alpha \tag{51}$$

with

$$\varepsilon_R = n_R^2 - n_I^2$$

$$= n^2 - (\frac{\lambda}{4\pi})^2\ \alpha^2 \tag{52}$$

$$\varepsilon_I = 2n_R n_I = 2n(\frac{\lambda}{4\pi})\,\alpha \tag{53}$$

where the subscripts R and I stand for real and imaginary parts, and n and α are defined in equation (22). Thence, the change in the real and imaginary parts of the dielectric constant of the medium is equivalent to the change in the real index of refraction and absorption coefficient of that medium. Knowledge of either change displays the optical properties of the medium investigated.

The scattering efficiency was measured to be approximately 10^{-3}. Using equation (50) and the excited-state absorption results reported in reference 30, the first term in equation (38) representing the contribution to the scattering due to an absorption grating can be calculated. Then using this result and the measured value of η in equation (38) the second term in brackets, which represents the contribution to the scattering due to a phase grating, can be estimated. The calculated values of $\Delta\alpha$ and Δn are given in Table XIII. Notice that the ions in inversion sites have longer lifetime than those in mirror sites

TABLE XIII

SUMMARY OF RESULTS OF FWM MEASUREMENTS
ON ALEXANDRITE

Parameter	Excitation Wavelength (nm) 488.0	514.5	579.1
η	$\sim 10^{-3}$	$\sim 10^{-3}$	$\sim 10^{-3}$
$I_o (W/cm^2)$	60	60	12
τ_{21} (ms)	49.13	50.27	0.30
$\bar{\alpha} (cm^{-1})$	0.36	0.54	2.80
$\Delta\alpha$ (cm^{-1})	2.62×10^{-3}	0.0	-0.87×10^{-3}
Δn	6.74×10^{-5}	7.78×10^{-5}	27.16×10^{-5}
$N_{2p} (cm^{-3})$	8.74×10^{17}	13.13×10^{17}	0.53×10^{17}

(Table XIII). Consequently, when exciting with the argon laser, the former ions contribute to the FWM signal for much longer time than the latter. This results in a negligible contribution of the latter. On the other hand, only the ions in mirror sites are excited when employing the ring dye laser. No contribution from the ions in inversion sites is obtained. Hence, in equation (50) we substitute for N_o the concentration of ions in inversion sites for argon laser excitation, and the concentration of ions in mirror sites for ring dye laser excitation.

In order to know which of the two terms of equation (38) dominates for various excitation wavelengths, the ratios of absorption to phase grating terms are calculated from this equation. For the three excitation wavelengths used in this study, the ratios are: 30.0×10^{-5} (λ_{ex} = 488.0 nm), 0.0 (λ_{ex} = 514.5 nm), and 0.30×10^{-5} (λ_{ex} = 579.1 nm). These results clearly show the minute contribution of the absorption grating term. In other words, the four-wave mixing signal in alexandrite is due mainly to scattering from a phase grating irrespective of what pump or probe wavelength (which are the same in our experiments) was utilized.

Using equation (50), the concentration of excited ions at the grating peak in either type of sites, i.e., N_{2p} can be calculated. The results are listed in Table XIII. These calculations show that 13%, 19% and 0.22% of the ions which are excited are, respectively, at the peak of the grating for λ_{ex} = 488.0, 514.5, and 579.1 nm. Figure 15 shows little absorption for the first two excitation wavelengths and significant absorption for the last one, however! The pumping intensity of the ions in inversion sites is five times as that of the ions in mirror sites. On the other hand, the absorption cross section of the former ions is

much less than (~20%) that of the latter. However, the ions in inversion sites have much longer lifetime (~160 times) than those in mirror sites have. All of this explains the order of magnitude larger concentration of excited ions (at the peak) at the argon laser excitation than at the ring dye laser excitation.

On the other hand, Fayer and coworkers [38] assumed the absence of excited-state absorption for the samples they studied. Consequently, for $\sigma_2 = 0$ equation (50) reduces to

$$2\,\Delta\alpha = -\sigma_1\, N_{2p} \tag{54}$$

which is the same as equation (45) identifying $\sigma_1 = \alpha_o/N_o$. Equation (44) predicts that phase grating contribution is minimal (zero) near (at) the absorption peak (here, 590.4 nm). For $\lambda_{ex} = 579.1$ nm, equation (54) gives $\Delta\alpha = -2.72 \times 10^{-3}$ cm^{-1} and subsequently, equation (38) gives $\Delta n = 27.16 \times 10^{-5}$, both of which are close to those listed in Table XIII obtained without the $\sigma_2 = 0$ assumption. This ensues in a ratio of the absorption to phase grating terms which is equal to 0.28×10^{-4} in concurrence with our previous conclusion: the scattering is due mainly to a phase grating even for probe or excitation wavelength close to absorption peak. However, when equations (44) and (45) are used with the experimental value of α_o obtained from the absorption spectrum in Figure 15, we obtain $\Delta\alpha_{ex} = 2.38 \times 10^{-3}$ cm^{-1} and $\Delta n_{ex} = 2.97 \times 10^{-9}$ which gives a ratio of absorption to phase grating terms equal to 1.79×10^{5}, signifying an overwhelming absorption grating contribution to scattering in agreement with the predictions of equation (44).

The sheer disagreement with the results obtained employing Hill's

approach (for $\Delta\alpha$) may be attributed to the fact that the workers of reference 38 assumed a damped oscillator model and moreover, considered the mere contributions of those transitions very close to the absorption peak neglecting excited-state absorption. Although those assumptions may be true for the samples investigated by them, they do not, however, apply to the alexandrite case. In alexandrite, excited-state absorption is significant and is, in our case, not much different from that of the ground state [30]. Hence, it cannot be neglected. The modulation of the absorption coefficient, $\Delta\alpha$ is explicitly a function of the difference in absorption cross section between the ground and excited states. Moreover, $\Delta\alpha$ depends on the fluorescence decay time of the excited (metastable) state. However, equation (50) shows no explicit dependence of $\Delta\alpha$ on the position of excitation (or probe) wavelength with respect to the absorption peak. The approach of Hill, though does not predict an expression for Δn, seems to be direct and applicable to alexandrite, the cousin of ruby.

On the other hand, the four-wave mixing signal efficiency is approximately the same as that of a similar sample of ruby. FWM in ruby has been investigated by several workers [24, 42-45] and the signal has been attributed to a Cr^{3+} population grating as proposed here. However, those workers disagree as to whether scattering is due to an absorption or phase grating.

In the alexandrite crystal under study, the scattering efficiency saturates (versus power) for small pump beam crossing angles and does not for large angles. This may be attributed to the efficiency of coupling the light into the solid. Effectively, more power is pumped into the sample at $\theta = 6°$ than at $\theta = 26.5°$, and this is due to having less reflection loss at small angles of incidence than at large ones.

CHAPTER IV

FOUR-WAVE MIXING STUDY IN NdP_5O_{14} CRYSTALS

A. Introduction

The stoichiometric rare-earth crystal neodymium pentaphosphate (NdP_5O_{14}) has been the object of extensive research after its emergence as a good mini-laser material [47-49] with weak concentration quenching. On the other hand, four-wave mixing has proved to be a powerful technique to unravel spatial migration of energy although spectral diffusion may not occur [20,50,51]. Exciton diffusion in NdP_5O_{14} has been recently addressed [52] and interpreted within the approach of Wong and Kenkre [53,54].

In this chapter, we present the data taken in attempt to identify the "mobility edge" in NdP_5O_{14}. At 11.5 K the diffusion coefficient varies linearly with the concentration of Nd^{3+} ions raised to the four thirds power as the excitation wavelength is scanned throughout the absorption band centered about 580 nm.

B. Experimental

High-quality single crystals of NdP_5O_{14} were grown by Philips Laboratories [55]. The sample investigated here was cleaved (5x5 mm) with a thickness of about 1 mm. In contrast to the degenerate four-wave mixing (DFWM) used in Chapter III (Figure 13), NdP_5O_{14} was investigated employing nondegenerate four-wave mixing configuration. The experimental setup is

illustrated in Figure 19. Two pump beams P_1 and P_2 interfere in the sample establishing a population grating. A probe beam P_r (of different wavelength) is directed in the region of interference at an angle $\sim 1^o$ with P_1. When the Bragg condition is satisfied, the probe beam scatters off this grating and emerges in a conjugate direction to pump beam P_2, giving rise to the FWM signal sought. The different (red) color of the (He-Ne laser) probe beam facilitated the visual detection of the FWM signal buried in the (mostly) yellow-background of scattered light. Moreover, the probe beam is not absorbed by the crystal (λ=632.8 nm), and hence is not attenuated.

The absorption spectrum of NdP_5O_{14} at room temperature is shown in Figure 20. It was taken on a Perkin-Elmer spectrophotometer with a resolution better than 0.07 nm. Decay rates were measured at room (296 K) and low temperatures (11.5 K). In the latter case, the sample was mounted in a cryogenic refrigerator. The signal-to-noise ratio was very good because of the double averaging achieved utilizing the Boxcar Integrator and Signal Averager (both manufactured by PAR). The grating was aligned along the a-axis of the crystal along which the diffusion of energy is maximum [56-59].

C. Data and Interpretation

The energy levels of Nd^{3+} ion in NdP_5O_{14} are given in ref. 52. In this study, the dye laser pumps the Nd^{3+} ions in the levels (slightly) above the metastable state $^4F_{3/2}$ ($\sim$16950-17500 cm^{-1}). Radiationless relaxation from these levels into the $^4F_{3/2}$ takes place very quickly and the latter fluoresces by relaxing to the ground state (^4I_j). Diffusion

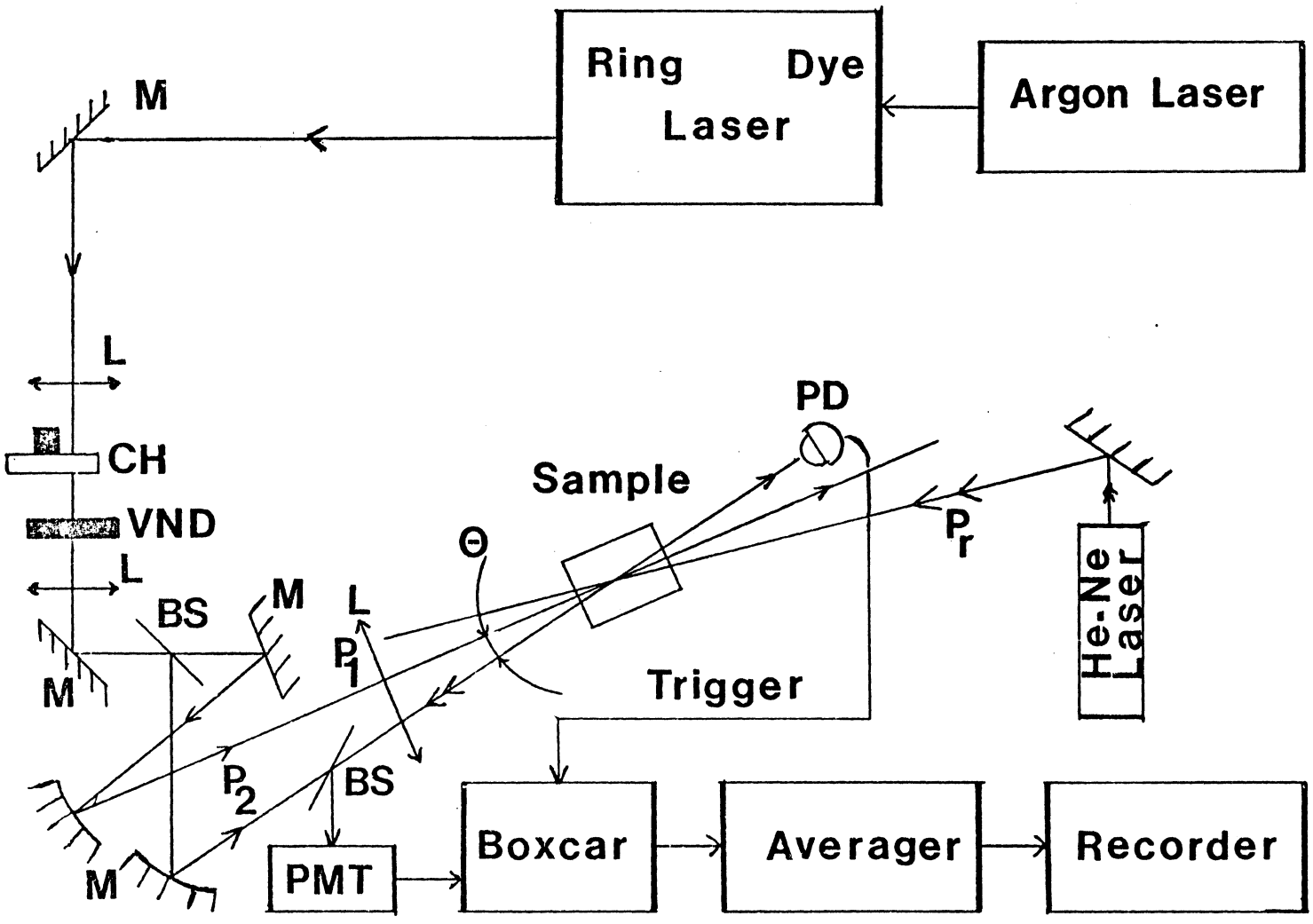

Figure 19. Nondegenerate four-wave mixing experimental setup for NdP_5O_{14}

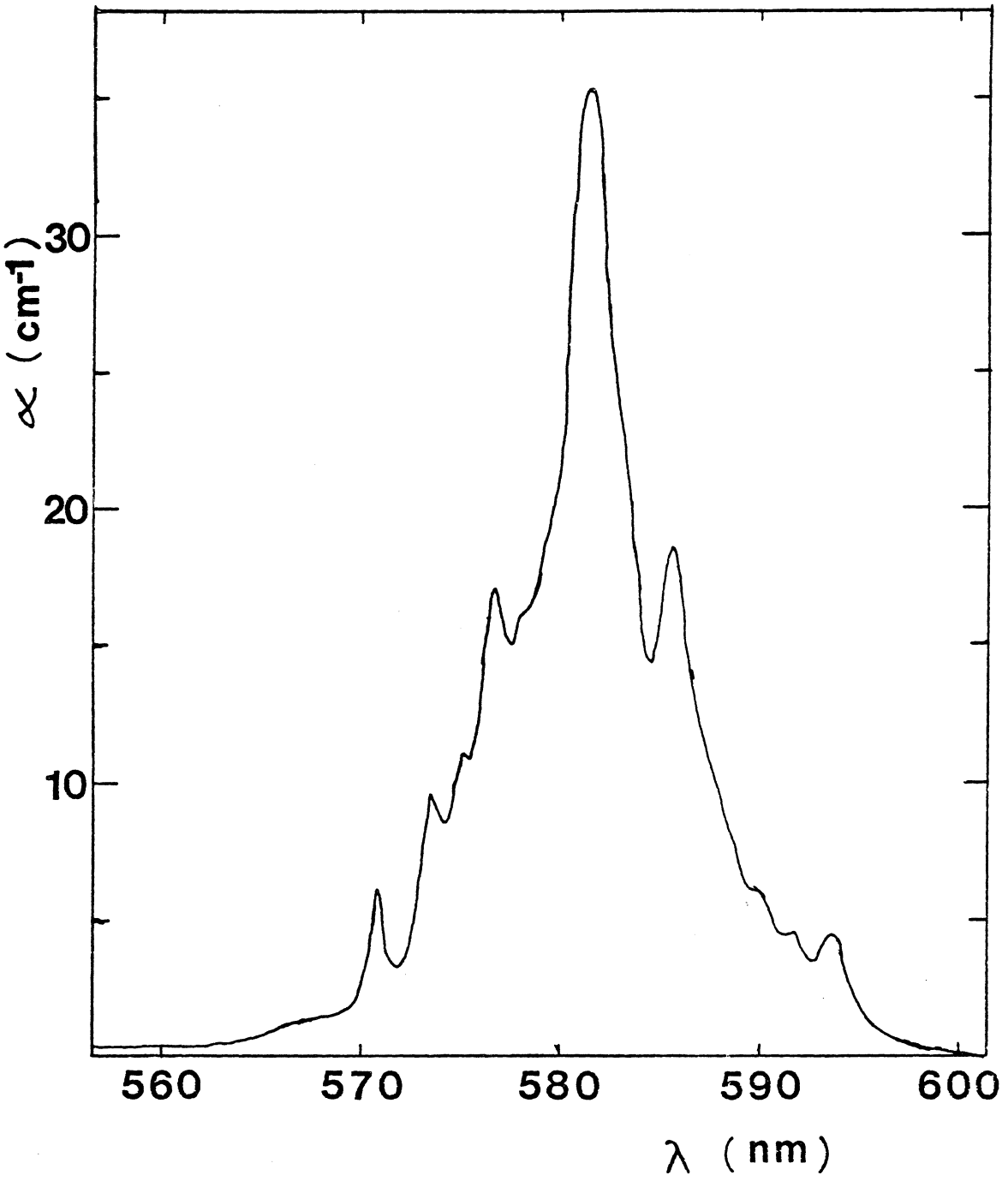

Figure 20. Absorption spectrum of NdP_5O_{14} at room temperature (Resolution is better than 0.07 nm)

of excitation energy occurs when the Nd^{3+} ions are in the $^4F_{3/2}$ metastable state.

Once the excitation intensity is cut off (by chopper), the grating starts to fade away as a result of the finite fluorescence lifetime of the excited state and of the migration of the excitation energy from the maxima regions of the grating to the minima. If the migration of energy is diffusive, then the diffusion coefficient is given by

$$D = (\tau_g^{-1} - 2\tau_f^{-1}) \lambda^2/(32\pi^2 \sin^2\Theta/2) \qquad (55)$$

where τ_g and τ_f are, respectively, the grating and excited-state fluorescence decay times, λ is the excitation wavelength, and Θ is the pump beams crossing angle.

Fluorescence lifetime measurements at room temperature for excitation wavelengths in the range 570-590 nm show insignificant variation of the fluorescence lifetime of the $^4F_{3/2}$ state with λ, and an average value of 113.94 μs is obtained. Low temperature variation is likewise with an average fluorescence lifetime of 119.62 μs. Moreover, one can claim that the fluorescence lifetime does not vary with temperature (within 5%) in agreement with the previously reported results [50,56,58]. Finally, all fluorescence decay patterns were single exponentials.

Equation (55) indicates that the grating decay rate decreases with Θ attaining a minimum value of twice the fluorescence decay rate (Θ=0). This angular dependence was checked for several excitation wavelengths in order to be able to make use of equation (55) to calculate the diffusion coefficient. The laser wavelength was scanned through the absorption spectrum and the corresponding grating decay times were measured at

296 K and 11.5 K for $\Theta=9.5^{o}$. The values of the diffusion coefficient at both temperatures were calculated and are listed in Tables XIV and XV as D_{exp}; also listed are the values of the grating decay times τ_g. Figure 21 shows the variation of D with λ at both temperatures; also shown in the figure a portion of the absorption spectrum at room temperature. A prominent peak of absorption is centered about 581.5 nm. Correspondingly, the diffusion coefficient is maximum there, though not significantly at 296 K. The low temperature data show a rate of change of the diffusion coefficient analogous to that of the concentration of Nd^{3+} ions being absorbed.

Förster [9] derived an expression for the diffusion coefficient variation with the concentration of active ions in the case of electric dipole-dipole interactions. If a localized exciton diffuses from one site to another in a random walk pattern, then the diffusion coefficient (in NdP_5O_{14}) can be expressed as

$$D = (4\pi/3)^{4/3} \frac{R_o^6}{2\tau_o} N^{4/3} \qquad (56)$$

where R_o is the critical interaction distance defined in Equation (6), τ_o is the intrinsic fluorescence lifetime, and N is the concentration of Nd^{3+} ions in NdP_5O_{14} for a certain excitation wavelength.

In a crystal, the linewidth of the transition arising from the contribution of all ions will be inhomogeneously broadened when the energy levels of an ion depend on the position of that ion in the crystal. In other words, if the ions occupy different environments (sites) the transitions will be inhomogeneously broadened. In the case of NdP_5O_{14} we considered, as an approximation, one constant value of the absorption cross

TABLE XIV

VARIATION OF THE DIFFUSION COEFFICIENT WITH EXCITATION WAVELENGTH AT T=296 K

λ(nm)	τ_g(μs)	D_{exp}($10^{-6}cm^2/s$)
571.79	50.78	3.21
572.22	50.78	3.21
572.45	50.78	3.21
572.72	49.68	3.87
572.95	50.08	3.63
573.10	49.16	4.21
573.61	48.15	4.86
573.96	48.69	4.50
574.09	49.24	4.16
574.18	49.98	3.84
574.58	49.39	4.08
574.87	51.01	3.11
575.17	49.80	3.83
575.37	50.96	3.14
575.68	49.27	4.17
575.85	50.00	3.72
575.93	48.30	4.80
576.34	47.37	5.42
576.42	46.51	6.02
576.60	47.50	5.34
576.92	48.47	4.70
577.08	48.69	4.56
577.18	49.98	3.75
577.57	50.15	3.65
577.66	50.59	3.39
578.09	48.35	4.80
578.22	48.27	4.86
578.67	47.53	5.36

TABLE XIV (Continued)

λ(nm)	τ_g(μs)	D_{exp}(10^{-6} cm^2/s)
579.58	46.83	5.86
579.90	46.53	6.08
580.00	48.04	5.04
580.65	45.83	6.61
581.00	46.84	5.88
581.17	44.37	7.73
581.50	44.35	7.76
581.68	45.19	7.12
581.76	46.04	6.48
582.28	48.72	4.62
582.38	47.79	5.25
582.52	47.94	5.15
582.88	47.86	5.21
583.02	47.31	5.59
583.24	47.72	5.31
583.37	48.46	4.81
583.55	48.42	4.84
583.87	48.38	4.88
584.07	48.49	4.80
584.12	47.74	5.31
584.47	47.88	5.22
584.63	47.51	5.48
584.72	47.73	5.33
584.88	47.70	5.36
585.24	47.93	5.20
585.40	48.45	4.85
585.75	49.02	4.48
585.91	49.16	4.38

TABLE XIV (Continued)

λ(nm)	τ_g(μs)	D_{exp}($10^{-6}cm^2/s$)
585.98	49.89	3.92
586.17	50.50	3.54
586.50	50.73	3.40
586.58	51.05	3.21
587.01	50.71	3.42
587.30	51.08	3.20
587.62	51.66	2.85
587.87	51.91	2.71
588.29	52.53	2.35
588.75	53.45	1.83
589.00	52.96	2.11
589.32	52.32	2.48
590.12	52.00	2.67
590.16	52.00	2.67
590.61	52.00	2.67

TABLE XV

VARIATION OF THE DIFFUSION COEFFICIENT WITH EXCITATION WAVELENGTH AND CONCENTRATION OF Nd^{3+} IONS AT T=11.5 K

λ(nm)	τ_g(μs)	D_{exp}($10^{-6}cm^2/s$)	N($5x10^{19}cm^{-3}$)	D_{fit}($10^{-6}cm^2/s$)
571.79	56.37	1.54	0.29	0.46
572.22	56.37	1.54	0.32	0.53
572.45	56.37	1.54	0.42	0.89
572.72	55.77	1.82	0.60	1.22
572.95	55.25	2.09	0.76	1.66
573.10	54.95	2.24	0.83	1.87
573.61	54.23	2.61	0.94	2.21
573.96	54.41	2.51	0.87	1.99
574.09	54.29	2.57	0.87	1.99
574.18	53.71	2.88	0.87	1.99
574.58	53.59	2.95	1.01	2.42
574.87	53.35	3.08	1.12	2.78
575.17	52.98	3.28	1.08	2.66
575.37	52.55	3.52	1.10	2.74
575.68	52.68	3.45	1.19	3.02
575.85	52.00	3.83	1.30	3.41
575.93	50.91	4.46	1.32	3.65
576.34	50.80	4.53	1.66	4.70
576.42	50.65	4.62	1.68	4.78
576.60	50.69	4.60	1.69	4.82
576.92	50.96	4.44	1.59	4.44
577.08	52.03	3.83	1.55	4.30
577.18	52.28	3.69	1.52	4.20
577.57	52.74	3.44	1.53	4.22
577.66	52.29	3.69	1.55	4.30
578.09	52.24	3.72	1.61	4.50
578.22	49.29	5.49	1.62	4.56
578.67	48.69	5.88	1.73	4.97

TABLE XV (Continued)

λ(nm)	τ_g(μs)	D_{exp}($10^{-6}cm^2/s$)	N($5x10^{19}cm^{-3}$)	D_{fit}($10^{-6}cm^2/s$)
578.75	48.40	6.07	1.75	5.04
579.58	48.62	5.91	2.04	6.19
579.90	46.37	7.49	2.18	6.77
580.00	47.12	6.97	2.22	6.94
580.65	45.60	8.08	3.21	11.33
581.00	43.66	9.60	3.43	12.36
581.17	41.34	11.60	3.46	12.50
581.50	41.31	11.64	3.50	12.70
581.68	42.44	10.64	3.46	12.50
581.76	44.44	9.00	3.43	12.36
582.28	46.42	4.52	2.85	9.67
582.38	48.79	5.89	2.74	9.17
582.52	51.62	4.14	2.67	8.86
582.88	51.74	4.07	2.38	7.60
583.02	50.82	4.62	2.29	7.22
583.24	50.40	4.88	2.16	6.67
583.37	51.10	4.46	2.06	6.26
583.55	51.86	4.01	1.88	5.57
583.87	53.08	3.32	1.64	4.63
584.07	53.08	3.32	1.55	4.30

section throughout the absorption spectrum and calculated the values of ion concentration for every data point. These are listed in Table XIII. A plot of D versus $N^{4/3}$ gives the value of the quantity multiplying the latter in equation (56). The best value is obtained using the least squares method. Using the values of N at room temperature, the fitted values of D can be obtained. The low temperature fit data points are listed in Table XV as D_{fit}. The dashed line in Figure 21 represents the theoretical fit and shows a good fit to the low temperature data. At low temperature, the linewidths of transitions are sharp and one can identify the individual transitions. This is not possible at room temperature because of the broadening and overlap of the transitions. Hence, using low temperature values of N is expected to lead to a better fit to the data. On the other hand, room temperature data do not indicate the behavior implicated by equation (56). Moreover, equation (56) implies that the diffusion coefficient increases when the concentration of ions, excited by the narrow-line laser, increases and vice versa. This is obvious in the profile of D following exactly that of N (versus excitation wavelength). This agrees with what has been suggested in ref. 52: the diffusion coefficient increases in the regions where the laser excitation wavelength is in resonance with the transitions of those excited ions.

There was no abrupt change in the value of D in the whole range of excitation considered in this study. The transition from the region of localized states to that of nonlocalized states is an Anderson transition [60], and the energy at which this occurs is called the mobility edge [61]. For NdP_5O_{14}, electric dipole-dipole interactions are expected and hence no sharp changes in the mobility will arise. In other words, no mobility

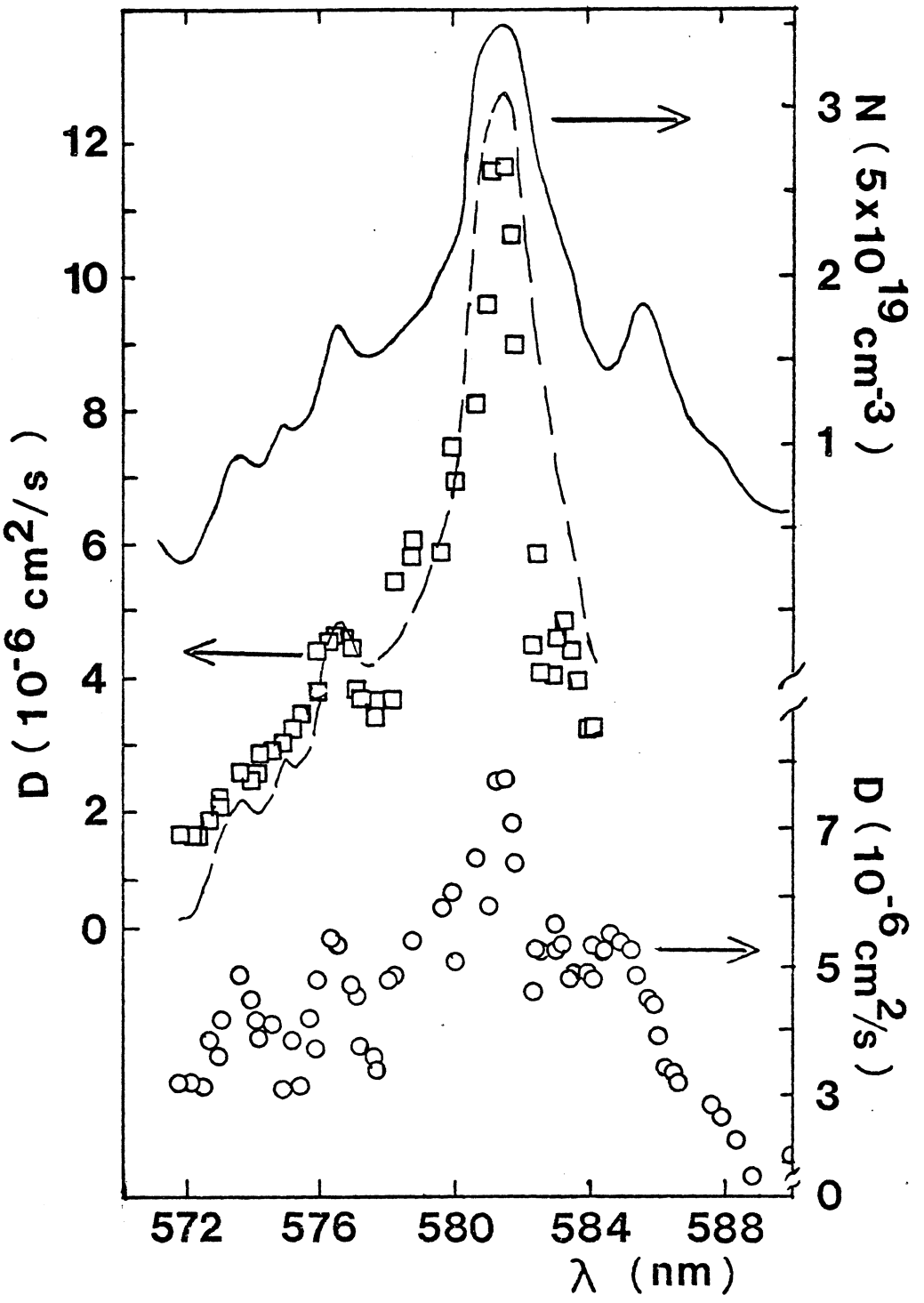

Figure 21. Variation of the diffusion coefficient with excitation wavelength at 296 K (○) and 11.5 K (□). The dashed line is the theoretical fit. The upper diagram is a portion of the absorption spectrum at room temperature

edge is expected in this crystal. This is verified by the low temperature data where D is proportional to $N^{4/3}$ which is characteristic of dipole-dipole interactions.

At T=11.5 K with high laser power, an interesting phenomenom was observed. In the region of 584-587 nm, the signal used to increase, decrease and then disappear. This happened every time the laser was tuned in that region. Furthermore, when the exciting laser was tuned further in the absorption band towards red no signal was observed.

For low temperature and low laser power, the oscillatory patterns reported in ref. 52 were not observed. Instead, exponential decays were obtained. No immediate explanation of this can be given. On the other hand, for λ=581.5 nm the signal grew gradually for a power decrease of 20%, and when the power was reduced by 30% the signal was reduced by 50% and it then disappeared in about 30 seconds. This behavior was consistently observed at the same laser excitation wavelength and power. This also occurred for λ=582.64 nm. No signal was observed for any larger value of λ. Presently, there is not sufficient data which would lead to a definitive statement of what causes that. NdP_5O_{14} has ferroelastic domains which are easy to distrub by applying little stress on the sample. Internal stress may arise when the laser power is directed into the sample which may displace these ferroelastic domains and give rise to changes in the region where the grating is established. The probe beam "sees" a distorted grating and scatters off it. More work needs to be done before we can claim that, and this will be the subject of future research in NdP_5O_{14} crystal.

CHAPTER V

SUMMARY AND CONCLUSIONS

A. Summary

In s mary, the results in Chapter II show the complex nature of the dynamics the interaction among clusters of Eu^{2+} ions occupying three different ypes of sites in $RbMgF_3$ crystals. The picture most consistent with all the data is that the sensitizer transfers energy to the high energy ac vator from its upper crystal field state as it relaxes from the excit $^6P_{7/2}$ level. At low temperature this activator either transfers the ergy on to the low temperature activator which fluoresces or back tran ers to the sensitizer, whereas at high temperature it either fluoresce itself or back transfers. The transfer process is consistent with elec ic dipole-dipole interaction and is enhanced by the thermal occupatio of the upper crystal field component of the sensitizer. The microscop origin of the different types of sites is not known but is probably e to the presence of structural or chemical impurities in the lattice.

In C pter III, an expression for the scattering efficiency within a coupled-w e treatment has been derived. Two approaches for obtaining the absor ion and phase contributions to the scattering from a population grating w e presented. The results show a dominant phase grating contribution or all the wavelengths employed to excite the alexandrite

crystal. Moreover, the FWM signal efficiency varied quadratically with pump power at large crossing angles with some saturation at small angles. Surface data show deviations from both effects. Pump beam polarized parallel to the b-axis of alexandrite effected strong FWM signals, and very weak FWM signals were obtained when polarized parallel to the c-axis. No FWM signal could be detected for pump beam polarized parallel to the a-axis.

The E//b polarization direction which produced strong FWM signal is also the polarization orientation for laser action in alexandrite. This implies that the operation of alexandrite lasers at high powers may result in beam scattering through self-induced phase conjugation [62] or other nonlinear optical effects. For both ruby and alexandrite crystals, the laser-induced changes in the dielectric constant are significantly greater for the population gratings obtained through pumping the Cr^{3+} ions than those for intrinsic host crystal properties investigated by off-resonance pumping [63]. The nonlinear properties of the type investigated here are known to affect laser operational properties in ruby [64] and thus may also be important in alexandrite laser operation. Finally, thermal gratings with shorter, angular dependent decay rates were also observed in ruby [34] and will be the subject of a future investigation of alexandrite.

In Chapter IV, nondegenerate FWM technique was used to study the stoichiometric crystal, NdP_5O_{14}. The fluorescence of the $^4F_{3/2}$ state was (again) found to be independent of the excitation wavelength and temperature. Low temperature data show the direct dependence of the diffusion coefficient upon the concentration of Nd^{3+} ions selectively excited

by the laser, whereas room temperature data do not exhibit such a dependence. No mobility edge has been detected in NdP_5O_{14}, as expected.

B. Conclusions

In conclusion, this work demonstrates the usefulness of time-resolved site-selection energy transfer studies to elucidate impurity ion distributions in host crystals. In particular, the results show that Eu^{2+} ions are forming close neighbor clusters in $RbMgF_3$ crystals even at very low concentrations.

In addition, the versatility of the technique of four-wave mixing (whether degenerate or nondegenerate) transient-grating spectroscopy in studying nonlinear processes in alexandrite and exciton diffusion in NdP_5O_{14} was manifested. The population grating in alexandrite is primarily dispersive and the migration of energy in NdP_5O_{14} is primarily diffusive.

REFERENCES

1. Blasse, G. and A. Bril, Philips Techn. Rev. 31, 303 (1970).

2. Brixner, L. H., J. D. Bierlein and V. Johnson in Current Topics in Material Science, Vol. 4, edited by E. Kaldis (North-Holland, New York, 1980) p. 47.

3. Garcia-Sole, J., M. Aguilar G., F. Agullo-Lopez, H. Murrieta S. and J. Rubio O, Phys. Rev. B 26, 3320 (1982).

4. Lopez, F. J., H. Murrieta S., J. Hernandez A. and J. Rubio O., Phys. Rev. B 22, 6428 (1980).

5. Rodriguez, F., M. Moreno, F. Jaque and F. J. Lopez, J. Chem. Phys. 78, 73 (1983).

6. Pascual, J. L., L. Arizmendi, F. Jaque and F. Agullo-Lopez, J. Lumin. 17, 325 (1978).

7. Merkle, L. D., R. C. Powell and T. M. Wilson, J. Phys. C 11, 3103 (1978).

8. Shinn, M. D. and W. A. Sibley, Phys. Rev. B 29, 3834 (1984).

9. Förster, T., Ann. Phys. 2, 55 (1948); Z. Naturforsch 49, 321 (1949).

10. Dexter, D. L., J. Chem. Phys. 21, 836 (1953).

11. Powell, R. C. and G. Blasse, Structure and Bonding 42, 43 (1980).

12. Inokuti, M. and F. Hirayama, J. Chem. Phys. 43, 1965 (1978).

13. Koumvakalis, N. and W. A. Sibley, Phys. Rev. B 13, 4509 (1976).

14. Rubio O., J., H. Murrieta S., E. Muñoz P., J. Boldú O. and G. Aguillar S., J. Chem. Phys. 63, 4222 (1975).

15. DiBartolo, B., Optical Interactions in Solids (Wiley, New York, 1968).

16. Holt, E. M., Unpublished Results, Oklahoma State University, Chemistry Department.

17. Hellwarth, R. W., J. Opt. Soc. Am. 67, 1 (1977).

18. Yariv, A. and D. M. Pepper, Opt. Lett. 1, 16 (1977).

19. Abrams, R. L. and R. C. Lind, Opt. Lett. 2, 94 (1978); 3, 205 (1978).

20. Lawson, C. M., R. C. Powell and W. K. Zwicker, Phys. Rev. B 26, 4836 (1982).

21. Liao, P. F. and D. M. Bloom, Opt. Lett. 3, 4 (1978).

22. Tyminski, J. K., Energy Migration Processes in Rare Earth Pentaphosphates. Ph.D. Thesis, Oklahoma State University, 1983.

23. Salcedo, J. R., A. E. Seigman, D. D. Dlott and M. D. Fayer, Phys. Rev. Lett. 41, 131 (1978).

24. Walling, J. C., O. G. Peterson, H. P. Jenssen, R. C. Morris and E. W. O'Dell, IEEE J. Quant. Elect. QE-16, 1302 (1980).

25. Walling, J. C., H. P. Jenssen, R. C. Morris, E. W. O'Dell and O. G. Peterson, Opt. Lett. 4, 182 (1979).

26. Walling, J. C. and L. Horowitz, Lasers '80, edited by C. B. Collins, (STS, McLean, 1980), p. 534.

27. Walling, J. C. and O. G. Peterson, IEEE J. Quant. Elect. QE-16, 119 (1980).

28. Cline, C. F., R. C. Morris, M. Dutoit and P. J. Harget, J. Mat. Sci. 14, 941 (1979).

29. Shand, M. L., J. Appl. Phys. 54, 2602 (1983).

30. Shand, M. L., J. C. Walling and R. C. Morris, J. Appl. Phys. 52, 953 (1981).

31. Sevast'yanov, B. K., Yu. I. Remigailo, V. P. Orekhova, V. P. Matrosov, E. G. Tsvetkov and G. W. Bukin, Sov. Phys. Dokl. 26, 62 (1981).

32. Walling, J. C., Laser Focus 19, 45 (1982).

33. Kogelnik, H., Bell. Sys. Tech. J. 48, 2909 (1969).

34. Eichler, H. and H. Stahl, J. Appl. Phys. 44, 3429 (1973); Eichler, H., G. Salje and H. Stahl, J. Appl. Phys. 44, 5383 (1973).

35. Nelson, K. A. and M. D. Fayer, J. Chem. Phys. 72, 5202 (1980).

36. Nelson, K. A., D. R. Lutz, M. D. Fayer and L. Madison, Phys. Rev. B 24, 3261 (1981).

37. Nelson, K. A., R. J. Dwayne Miller, D. R. Lutz and M. D. Fayer, J. Appl. Phys. 53, 1144 (1982).

38. Nelson, K. A., R. Casalegno, R. J. Dwayne Miller and M. D. Fayer, J. Chem. Phys. 77, 1144 (1982).

39. Dwayne Miller, R. J., R. Casalegno, K. A. Nelson and M. D. Fayer, Chem. Phys. 72, 371 (1982).

40. Fayer, M. D., Ann. Rev. Phys. Chem. 33, 63 (1982).

41. Farrell, E. F., J. H. Fang and R. E. Newnham, Amer. Miner. 48, 804 (1963).

42. Eichler, H. J., J. Eichler, J. Knof and Ch. Noak, Phys. Stat. Sol. (a) 52, 48 (1979).

43. Hill, K. O., Appl. Opt. 10, 1695 (1971).

44. Hamilton, D. S., D. Heiman, J. Feinberg and R. W. Hellwarth, Opt. Lett. 4, 124 (1979).

45. Liao, P. F., L. M. Humphrey, D. M. Bloom and S. Geschwind, Phys. Rev. B 20, 4145 (1979); Liao, P. F. and D. M. Bloom, Opt. Lett. 3, 4 (1978).

46. Kroll, N. M., J. Appl. Phys. 36, 34 (1965).

47. Danielmeyer, H. G. and H. P. Weber, IEEE J. Quant. Elect. QE-8, 805 (1972).

48. Danielmeyer, H. G., Festkörperprobleme 15, 253 (1975).

49. Weber, H. P., Opt. Quant. Electron 7, 431 (1975).

50. Flaherty, J. M. and R. C. Powell, Phys. Rev. B 19, 32 (1979).

51. Lawson, C. M., R. C. Powell and W. K. Zwicker, Phys. Rev. Lett. 46, 1070 (1981).

52. Tyminski, J. K., R. C. Powell and W. K. Zwicker, Phys. Rev. B 29, 6074 (1984).

53. Wong, Y. M. and V. M. Kenkre, Phys. Rev. B 22, 3072 (1980).

54. Kenkre, V. M., Phys. Rev. B 18, 4064 (1978).

55. Plattner, R. D., W. W. Krühler, W. K. Zwicker, T. Kovats, and S. R. Chinn, J. Cryst. Growth 49, 274 (1980).

56. Huber, G., W. W. Krühler, W. Bludau and H. G. Danielmeyer, J. Appl. Phys. 46, 3580 (1975).

57. Danielmeyer, H. G., J. P. Jeser, E. Schönherr and W. Stetter, J. Cryst. Growth 22, 298 (1974).

58. Blätte, H. G. Danielmeyer, and R. Ulrich, Appl. Phys. 1, 275 (1973).

59. Albrand, K. R., R. Attig, J. Fenner, J. P. Jeser and D. Mootz, Mat. Res. Bull. 9, 129 (1974).

60. Anderson, P. W., Phys. Rev. 109, 1492 (1958).

61. Cohen, M. H., H. Fritzche and S. R. Ovshinsky, Phys. Rev. Lett. 22, 1065 (1969); Mott , N. F., Adv. Phys. 16, 49 (1967).

62. Feinberg, J., Optical Phase Conjugation, edited by R. A. Fisher (Academic Press, N. Y., 1983), p. 417.

63. Weber, M. J., D. Milam and W. L. Smith, Opt. Eng. 17, 463 (1978).

64. Eichler, H., P. Glozbach and B. Kluzowski, Z. Agnew. Physik 28, 303 (1970).

APPENDIX

Excited-state (population) gratings were treated in Chapter III of this thesis. However, one can also use four-wave mixing techniques to observe thermal gratings. Despite the fact that these were not observed in our experiments on alexandrite, since they are very fast on the time scale of the experiments, it is rather informative and surely complementary to present a survey of the methods of generation of these gratings and their implications.

Recently, ultrasonic waves were generated by optical excitation employing a picosecond transient-grating technique [23] called Laser Induced Phonon Spectroscopy (LIPS). In LIPS experiments [35-40], two picosecond laser excitation pulses, of wavelength λ, cross in the bulk of the sample at an angle θ. The optical properties of the sample in the ground and excited states are now altered and a grating of period $\Lambda = \lambda/2 \sin(\theta/2)$ is established. A third probe pulse Bragg diffracts off of the grating and the diffracted signal whether is due to an excited-state grating, an acoustic-wave grating, or both is detected.

Two approaches to the generation of acoustic waves have been suggested. In absorbing samples, radiationless relaxation sets up a temperature distribution and thermal expansion starts ultrasonic waves of definite wave vector. On the other hand, in transparent (or weakly absorbing) samples, the optical electromagnetic excitation field couples electrostrictively to the acoustic field of the sample. In this

Appendix, the two approaches are presented, viz., the heating mechanism and the electrostrictive (Stimulated Brillouin Scattering) mechanism.

Heating Mechanism

Assume the excitation into the vibrational states of the excited state of dopant ion in a crystal host [35]. Moreover, a subsequent radiationless relaxation induces a temperature distribution oscillating with the period of the interference pattern set up by the two crossed excitation pulses. The latter (80 psec) and relaxation are instantaneous on the experiment time scale (~50 nsec). If Q cal/ion is the heat deposited into the crystal, then the spatially varying temperature increase is given by (in the y-direction).

$$\Delta T(y) = \frac{Q\beta}{\rho_o C_v} I(r) = \frac{Q\beta}{\rho_o C_v} \frac{I_{max}}{2} (1+\cos ky)$$

$$\Delta T(y) = \frac{\Delta T_{max}}{2} (1+\cos ky) \qquad \text{(A-1)}$$

where I(r) is the total intensity per/laser pulse in the interference region with a maximum integrated value I_{max}, $\beta(cm^{-1})$ is the absorption per unit thickness of sample, $\rho_o(g/cm^3)$ is the crystal density, C_v(cal/g K) is the constant volume heat capacity, and $k = \frac{2\pi}{\Lambda}$ is the grating wave vector.

The dynamics and thermal expansion can be described by the constitutive equation of motion [35]

$$\underset{\sim}{T} = \underset{\sim}{c}\,\underset{\sim}{S} \quad \text{or} \quad \underset{\sim}{S} = \underset{\sim}{s}\,\underset{\sim}{T} \quad (\underset{\sim}{s} = \underset{\sim}{c}^{-1}) \qquad \text{(A-2)}$$

and the strain-displacement relation (in the Hooke's law elastic limitation)

$$\nabla \cdot \underset{\sim}{T} = \rho_o \partial_t^2 \vec{u} - \vec{F} = \rho_o \partial_t \vec{v} - \vec{F} \qquad \text{(A-3)}$$

where,

$$\nabla\cdot = \begin{bmatrix} \partial_x & 0 & 0 & 0 & \partial_z & \partial_y \\ 0 & \partial_y & 0 & \partial_z & 0 & \partial_x \\ 0 & 0 & \partial_z & \partial_y & \partial_x & 0 \end{bmatrix} = \nabla_s^+ \qquad \text{(A-4)}$$

$\underset{\sim}{T}$ and $\underset{\sim}{S}$ are, respectively, the stress and strain 6 x 1 vectors, $\underset{\sim}{c}$ and $\underset{\sim}{s}$ are, respectively, the elastic stiffness and compliance 6 x 6 symmetric matrices, $\vec{u}$ and $\vec{v}$ are, respectively the displacement and velocity vectors, and $\vec{F}$ represents the applied body forces given by

$$\vec{F} = -\nabla\cdot\underset{\sim}{T} = -\nabla\cdot(\underset{\sim\sim}{c}\underset{\sim}{\alpha}\Delta T) \qquad \text{(A-5)}$$

where $\underset{\sim}{\alpha}$ is the thermal expansion (6 x 1) vector. The above is due to thermal-expansion induced stress (and strain). Substituting in equation (A-3) one obtains

$$\nabla\cdot\underset{\sim}{T} = \rho_o\, \partial_t\, \vec{v} + \nabla\cdot(\underset{\sim\sim}{c}\underset{\sim}{\alpha}\Delta T) \qquad \text{(A-6)}$$

The strain is related to displacement and velocity by

$$\underset{\sim}{S} = \nabla_s\, \vec{u} \quad \text{or} \quad \partial_t\, \underset{\sim}{S} = \nabla_s\, \vec{v} \qquad \text{(A-7)}$$

Using equation (A-2), one has

$$\partial_t \underset{\sim}{T} = \underset{\sim}{c}\, \nabla_s\, \vec{v} \qquad \text{(A-8)}$$

with the boundary conditions $\underset{\sim}{T}(0)=0$ and $\vec{v}(0)=0$, one solves the acoustic problem by solving equations (A-6) and (A-8).

Consider the case when the grating is aligned along the b-axis (i.e. y-axis) of a monoclinic system (crystal). The stiffness and thermal expansion tensors are given by

$$\underset{\sim}{c} = \begin{bmatrix} c_{11} & c_{12} & c_{13} & 0 & c_{15} & 0 \\ c_{12} & c_{22} & c_{23} & 0 & c_{25} & 0 \\ c_{13} & c_{23} & c_{33} & 0 & c_{35} & 0 \\ 0 & 0 & 0 & c_{44} & 0 & c_{46} \\ c_{15} & c_{25} & c_{35} & 0 & c_{55} & 0 \\ 0 & 0 & 0 & c_{46} & 0 & c_{66} \end{bmatrix}, \quad \underset{\sim}{\alpha} = \begin{bmatrix} \alpha_1 \\ \alpha_2 \\ \alpha_3 \\ 0 \\ \alpha_5 \\ 0 \end{bmatrix} \qquad \text{(A-9)}$$

Since $\vec{v} = v_y(y)\hat{y}$, equation (A-6) becomes

$$\begin{bmatrix} \partial_x & 0 & 0 & 0 & \partial_z & \partial_y \\ 0 & \partial_y & 0 & \partial_z & 0 & \partial_x \\ 0 & 0 & \partial_z & \partial_y & \partial_x & 0 \end{bmatrix} \begin{bmatrix} T_1 \\ T_2 \\ T_3 \\ T_4 \\ T_5 \\ T_6 \end{bmatrix} = \rho_o \partial_t \begin{bmatrix} 0 \\ v_y \\ 0 \end{bmatrix} +$$

$$\begin{bmatrix} \partial_x & 0 & 0 & 0 & \partial_z & \partial_y \\ 0 & \partial_y & 0 & \partial_z & 0 & \partial_x \\ 0 & 0 & \partial_z & \partial_y & \partial_x & 0 \end{bmatrix} \begin{bmatrix} c_{11} & c_{12} & c_{13} & 0 & c_{15} & 0 & \alpha_1 \\ c_{12} & c_{22} & c_{23} & 0 & c_{25} & 0 & \alpha_2 \\ c_{13} & c_{23} & c_{33} & 0 & c_{35} & 0 & \alpha_3 \\ 0 & 0 & 0 & c_{44} & 0 & c_{46} & 0 \\ c_{15} & c_{25} & c_{35} & 0 & c_{55} & 0 & \alpha_5 \\ 0 & 0 & 0 & c_{46} & 0 & c_{66} & 0 \end{bmatrix} \Delta T(y)$$

$$\partial_x T_1 + \partial_z T_5 + \partial_y T_6 = 0$$

$$\partial_y T_2 + \partial_z T_4 + \partial_x T_6 = (c_{12}\alpha_1 + c_{22}\alpha_2 + c_{23}\alpha_3 + c_{25}\alpha_5)\left(\frac{-k\Delta T_{max}}{2} \sin ky\right) + \rho_o \partial_t v_y(y)$$

$$\partial_z T_3 + \partial_y T_4 + \partial_x T_5 = 0$$

Similarly, equation (A-8) gives

$$c_{12}\, \partial_y v_y = \partial_t T_1 \qquad c_{44}\, \partial_z v_y = 0 = \partial_t T_4$$

$$c_{22}\, \partial_y v_y = \partial_t T_2 \qquad c_{25}\, \partial_y v_y = \partial_t T_5$$

$$c_{23}\, \partial_y v_y = \partial_t T_3$$

where

$$\partial_x v_y = \partial_z v_y = 0, \quad \text{since} \quad \partial_x v_y = \partial_t \partial_x y = 0 \quad \text{and so on.}$$

Hence, the resulting equations are

$$\partial_y T_2 = \rho_o \partial_t v_y - (c_{11}\alpha_1 + c_{22}\alpha_2 + c_{23}\alpha_3 + c_{25}\alpha_5)\frac{k\Delta T_{max}}{2} \sin ky \qquad \text{(A-10-a)}$$

$$c_{22}\partial_y v_y = \partial_t T_2 \qquad \text{(A-10-b)}$$

$$c_{12}\partial_y v_y = \partial_t T_1 \qquad \text{(A-10-c)}$$

$$c_{23}\partial_y v_y = \partial_t T_3 \qquad \text{(A-10-d)}$$

$$c_{25}\partial_y v_y = \partial_t T_5 \qquad \text{(A-10-e)}$$

Solving (A-10-a) and (A-10-b):

$$\partial_y[c_{22}\ \partial_y\ v_y] = \partial_y[\partial_t\ T_2] = \partial_t[\partial_y\ T_2]$$

$$\partial_y^2\ v_y - \frac{\rho_o}{c_{22}}\partial_t^2 v_y = -(c_{11}\alpha_1 + c_{22}\alpha_2 + c_{23}\alpha_3 + c_{25}\alpha_5)\frac{k\Delta T_{max}}{2} \sin ky \qquad \text{(A-11)}$$

Equation (A-11) is a wave equation (inhomogeneous) whose solution is (using the boundary conditions $\underset{\sim}{T}(0) = 0$, $\vec{v}(0) = 0$)

$$v_y = -A \sin \omega t \sin ky$$

$$= \frac{A}{2}[\cos(\omega t - ky) - \cos(\omega t + ky)] \qquad \text{(A-12)}$$

where

$$\omega = k\sqrt{c_{22}/\rho_o} = V_s, \text{ the velocity of sound,}$$

and

$$A = (c_{12}\alpha_1 + c_{22}\alpha_2 + c_{23}\alpha_3 + c_{25}\alpha_5)(k\Delta T_{max})/2\omega\rho_o$$

Equation (A-10-b) then gives

$$T_2 = \int \partial_t\ T_2\ dt = \int c_{22}\ \partial_y\ v_y\ dt = \frac{c_{22}k}{\omega} A \cos ky\ (1 - \cos \omega t)$$

$$= \frac{c_{22}k}{\omega}\{A \cos ky - \frac{A}{2}[\cos(\omega t + ky) + \cos(\omega t - ky)]\} \qquad \text{(A-13)}$$

Similarly,

$$u_y = \int v_y dy = \frac{A}{\omega} \sin ky - \frac{A}{2\omega} [\sin(\omega t + ky) - \sin(\omega t - ky)] \quad (A\text{-}14)$$

Hence, the strain in the y direction (i.e. $S_2 \equiv S_{yy}$)

$$S_2 = \frac{T_2}{c_{22}} = \frac{Ak}{\omega} \cos ky (1 - \cos \omega t) \quad (A\text{-}15)$$

It is obvious from equations (A-12) - (A-14) that we have two counter-propagating waves with time independent terms in equations (A-13)-(A-15). The time independent term in equation (A-14) represents the displacement arising from the initial temperature jump and thermal expansion. It can be considered constant since it decays in the millisecond range while the experiment is on the nanosecond scale. Another interesting observation is that equation (A-12) suggests that once the compressional waves are generated, they continue to travel throughout the crystal and even outside the grating region. Pure longitudinal waves are generated because of aligning the grating along a symmetry axis direction.

The form of solution to equations (A-6) and (A-8) does not change for both isotropic and aniosotropic media. If phonons are generated in the ac(-xz) plane of the monoclinic crystal, a rotation of the coordinate system about the y-axis keeps the forms of $\underset{\sim}{c}$ and $\underset{\sim}{\alpha}$ (as given by equation (A-9)) the same. Now $v_y = 0$, v_x and $v_z \neq 0$. The 3 x 3 Rotation matrix about y is given by

$$A = \begin{bmatrix} \cos\phi & 0 & \sin\phi \\ 0 & 1 & 0 \\ -\sin\phi & 0 & \cos\phi \end{bmatrix}$$

Then the transfer matrix becomes

$$M_T = \begin{bmatrix} \cos^2\phi & 0 & \sin^2\phi & 0 & 2\cos\phi\ \sin\phi & 0 \\ 0 & 1 & 0 & 0 & 0 & 0 \\ \sin^2\phi & 0 & \cos^2\phi & 0 & -2\cos\phi\ \sin\phi & 0 \\ 0 & 0 & 0 & \cos\phi & 0 & -\sin\phi \\ -\cos\phi\ \sin\phi & 0 & \cos\phi\ \sin\phi & 0 & \cos^2\phi\ -\sin^2\phi & 0 \\ 0 & 0 & 0 & \sin\phi & 0 & \cos\phi \end{bmatrix} \quad \text{(A-16)}$$

and we have $\underset{\sim}{C}' = M_T \underset{\sim}{C}\, \tilde{M}_T = \underset{\sim}{C}$, and $\underset{\sim}{\alpha}' = \underset{\sim}{\alpha}$

In an analogous manner to the previous case, the solution becomes in some normal coordinate system with n = 1,2

$$v_n = \frac{A_n}{2} \left[\cos\left(\omega_n t - kx\right) - \cos\left(\omega_n t + kx\right)\right] \quad \text{(A-17)}$$

$$u_n = \frac{A_n}{\omega_n} \sin kx - \frac{A_n}{2\omega_n} \left[\sin\left(\omega_n t + kx\right) - \sin\left(\omega_n t - kx\right)\right] \quad \text{(A-18)}$$

$$T_n' = \frac{b_n k}{\omega_n} \left\{A_n \cos kx - \frac{A_n}{2} \cos\left[\left(\omega_n t + kx\right) + \cos\left(\omega_n t - kx\right)\right]\right\} \quad \text{(A-19)}$$

with $\omega_n = \pm k\sqrt{b_n/\rho_o} = V_{sn}$ and i = 1, 2, 3, 5

$$A_n = \alpha_n' \Delta T_{max}\, k/2\omega_n\rho_o$$

$$\alpha_i' = \alpha_x + \alpha_i\alpha_z$$

$$T_i' = T_1 + a_i T_5$$

$$u_i = u_x + a_i u_2$$

$$\alpha_x = c_{11}\alpha_1 + c_{12}\alpha_2 + c_{13}\alpha_3 + c_{15}\alpha_5$$

$$\alpha_z = c_{15}\alpha_1 + c_{25}\alpha_2 + c_{35}\alpha_3 + c_{55}\alpha_5$$

$$a_{1,2} = \frac{c_{55} - c_{11}}{2\, c_{15}} \pm \sqrt{\left(\frac{c_{55} - c_{11}}{2\, c_{15}}\right)^2 + 1}$$

The field equations are

$$c_{1i}\, \partial_x v_x + c_{i5}\, \partial_x v_z = \partial_t T_i$$

$$\partial_x T_1 = \rho_o \partial_t v_x - \frac{\alpha_x k \Delta T_{max}}{2} \sin kx$$

$$\partial_x T_5 = \rho_o \partial_t v_z - \frac{\alpha_z k \Delta T_{max}}{2} \sin kx$$

Equations (A-17) - (A-19) show that in the symmetry plane (ac) two pairs of counterpropagating waves are generated: quasilongitudinal (n = 1) and quasitransverse (n = 2). Each wave propagates with a definite phase velocity V_{sn}. Generally, two quasitransverse waves plus a quasilongitudinal wave will be generated having the same wave vector. The acoustic waves can be generated for any grating propagation direction.

Electrostrictive (Stimulated Brillouin Scattering) Mechanism

In transparent (weakly absorbing) samples [36], the excitation electromagnetic field couples directly to the acoustic field of the material via Stimulated Brillouin Scattering (SBS). In the latter mechanism, two crossing laser pulses of slightly different frequencies (or same frequency but the spread in frequency is broad enough to) generate phonons with a difference frequency. In other words, a higher-frequency photon from each pulse is annihilated to produce in the

sample a lower-frequency photon plus phonons of the difference frequency and wave vector. Standing waves are generated [37].

The interaction Lagrangian of the process can be written as [46]

$$L_{int} = -\frac{1}{8\pi} p_{ijkl} D_i D_j \partial_l u_k \tag{A-20}$$

where the summation over repeated indices is assumed, p_{ijkl} are the photoelastic coefficients, and D_i are the electric displacement components. The reciprocal dielectric constant is related to the p_{ijkl} coefficients by [46]

$$\delta\nu_{ij} = p_{ijkl} \partial_l u_k \tag{A-21}$$

Using Lagrangian equations of motion, one solves for u_k in equation (A-20) and obtains the following equations giving, respectively, the electromagnetic field effect on the acoustic field and the converse effect:

$$\rho\ddot{u}_i + \eta_{ij}\dot{u}_j - c_{ijkl} \partial_i\partial_k u_l = \frac{1}{8\pi} p_{klji} \partial_j D_k D_l \tag{A-22}$$

and

$$\frac{1}{c^2} \ddot{D}_i - \nu_{kj} (\delta_{ik} \nabla^2 - \partial_i\partial_k) D_j = p_{kjlm} (\delta_{ik} \nabla^2 - \partial_i\partial_k) D_j \partial_m u_l \tag{A-23}$$

where c_{ijkl} are the elastic stiffness coefficients, η_{ij} are the acoustic damping constants, and ρ is the sample density. No heating was assumed. Our interest is equation (A-22) giving the electromagnetic field effect on the acoustic field, which we will try to solve:

Consider two x_1-polarized pulses bisected by the x_3 axis and propagating in its direction. A Gaussian laser pulse is given by [36]

$$\hat{x}_1 \; D \; \sqrt{\pi}\,\Gamma\, e^{-(x_1^2 + x_2^2)/\omega_o^2} \; e^{-(t - t_o - \frac{n}{c} x_3)^2\Gamma^2/4} \cos[\omega_L(t-t_o) - k_3x_3]$$

where ω_o is the spot size, ω_L is the central frequency, Γ is the spectral width, and t_o determines when the pulse passes through the crystal. The total field of the two pulses crossing the crystal at $x_3 = 0$ has the amplitude

$$\hat{x}_1 \; E\, e^{-(t - t_o)^2\Gamma^2/4} \cos[\omega_L(t - t_o) \pm k_2x_2 - k_3x_3]$$

where the variations in the x_1 and x_2 directions were ignored, and $E = \sqrt{\pi}\; D\; \Gamma$. The + sign is for pulse 1 and the - sign for pulse 2. The electromagnetic field intensity is, then, given by

$$D_1^2 = E^2\, e^{-(t-t_o)^2\Gamma^2/2} \{\cos[\omega_L(t-t_o)+k_2x_2-k_3x_3]+\cos[\omega_L(t-t_o)-k_2x_2-k_3x_3]\}^2$$

$$= E^2\, e^{-(t-t_o)^2\Gamma^2/2} \{2 \cos k_2x_2 \;\; \cos[\omega_L(t-t_o)-k_3x_3]\}^2$$

$$= E^2\, e^{-(t-t_o)^2\Gamma^2/2} \{1 + \cos 2k_2x_2\} \{1 + \cos 2[\omega_L(t-t_o) - k_3x_3]\}$$

$$D_1^2 = E^2\, e^{-(t-t_o)^2\Gamma^2/2} \{1+\cos2[\omega_L(t-t_o)-k_3x_3](1+\cos2k_2x_2)+\cos2k_2x_2\} \quad \text{(A-24)}$$

Equation (A-24) is substituted in equation (A-22) neglecting the second noneffective (on the acoustic field) term. Moreover, by aligning the grating along a symmetry axis (pure modes), only the i = 2 terms

survive in equation (A-22):

$$\ddot{u}_2 - V_p^2 \partial_2^2 u_2 = \frac{-k_2 p_{1122} E^2}{4\pi\rho} e^{-(t-t_o)^2\Gamma^2/2} \sin 2k_2 x_2 \qquad \text{(A-25)}$$

where $V_p = \sqrt{c_{2222}/\rho}$ is the longitudinal wave velocity. The solution of equation (A-25) is given by

$$u_2(x_2,t) = \frac{1}{2V_p} \int_{-\infty}^{\infty} dt' \int_{x_2-V_p(t-t')}^{x_2+V_p(t+t')} \frac{-k_2 p_{1122} E^2}{4\pi\rho} [e^{-(t'-t_o)^2\Gamma^2/2} \sin 2k_2 x_2' dx_2'] \qquad \text{(A-26)}$$

$$= \frac{-k_2 p_{1122} E^2}{8V_p \pi\rho} \int_{-\infty}^{\infty} \frac{dt'}{2k_2} \{\cos 2k_2[x_2+V_p(t-t')] - \cos 2k_2[x_2-V_p(t-t')]\}$$

$$= \frac{-p_{1122} E^2}{8V_p \pi\rho} \sin 2k_2 x_2 \int_{-\infty}^{\infty} e^{-(t'-t_o)^2\Gamma^2/2} \sin 2k_2 V_p (t-t') dt'$$

Make a change of variable $\xi = t' - t_o$

$$u_2(x_2,t) = \frac{-p_{1122} E^2}{8V_p \pi\rho} \sin 2k_2 x_2 \int_{-\infty}^{\infty} e^{-\xi^2 \frac{\Gamma^2}{2}} \{-\sin 2k_2 V_p (t_o - t + \xi)\} d\xi$$

Make use of:

$$\int_{-\infty}^{\infty} e^{-q^2 x^2} \sin [p(x+\lambda)] dx = (\sqrt{\pi}/q) e^{\frac{-p^2}{4q^2}} \sin p\lambda$$

Hence,

$$u_2(x_2,t) = \frac{-p_{1122}E^2\sqrt{2/\pi}}{8V_p\rho\Gamma} \; e^{\frac{-2k_2^2V_p^2}{\Gamma^2}} \sin 2k_2x_2 \sin 2k_2V_p\,(t-t_o) \qquad \text{(A-27)}$$

which gives

$$S_{22} = \partial_2 u_2 = \frac{-p_{1122}E^2k_2\sqrt{2/\pi}}{4V_p\rho\Gamma} \; e^{\frac{-2k_2^2V_p^2}{\Gamma^2}} \cos 2k_2x_2 \sin 2k_2V_p\,(t-t_o) \qquad \text{(A-28)}$$

or

$$S_{22} = \frac{-p_{1122}E^2k_2}{2^{5/2}\rho\Gamma V_p\sqrt{\pi}} \; e^{\frac{-2k_2^2V_p^2}{\Gamma^2}} \{\sin [2k_2V_p(t-t_o) + 2k_2x_2] + \sin [2k_2V_p(t-t_o) - 2k_2x_2]\} \qquad \text{(A-29)}$$

indicating a standing wave pattern for $t >> 2/\Gamma$. For short pulses, the exponential term is about 1, giving a constant amplitude of S_{22}.

It is interesting to solve equation (A-25) for a square pulse driving term starting at $t = 0$. In similar steps to the above, the solution is

$$S_{22}(t<\tau_L) = \frac{-p_{1122}E^2}{8\pi\rho V_p^2} \{\cos 2k_2x_2 - \frac{1}{2} [\cos 2k_2(V_pt-x_2) + \cos 2k_2(V_pt+x_2)]\} \qquad \text{(A-30)}$$

$$S_{22}(t>\tau_L) = \frac{p_{1122}E^2}{16\pi\rho V_p^2}([\cos 2k_2(V_pt - x_2) + \cos 2k_2(V_pt + x_2)] - \{\cos 2k_2[V_p(t-\tau_L)-x_2] + \cos 2k_2[V_p(t-\tau_L)+x_2]\}) \qquad \text{(A-31)}$$

where τ_L is the square-pulse duration. Equation (A-30) shows that the amplitude remains constant within the duration of the pulse. On the other hand, equation (A-31) shows the disappearance of the static term

$\cos(2k_2x_2)$ after the excitation pulses leave the crystal.

However, this electrostrictive coupling does not explain the initial static offset term. Hence, if heating driving terms are considered, then the acoustic field equation in terms of strain S_{22} is given by

$$\partial_t^2 S_{22} - \frac{V_p^2}{\gamma} \partial_2^2 S_{22} + \frac{V_p^2 \alpha_{22}}{\gamma} \partial_2^2 T$$

$$= \frac{P_{1122}}{8\pi\rho_o} \partial_2^2 D_1^2 + \partial_2 \left[\frac{D_1^2}{8\pi\rho_o} \left(\frac{\partial \nu_{11}}{\partial T}\right) \partial_2 T\right] \qquad \text{(A-32)}$$

where $\gamma = C_p/C_v$, and the second term on the right hand side is due to electrocaloric effect and is negligible. The heat conduction equation is

$$\rho_o C_v \partial_t T - \kappa_{22} \partial_2^2 T + \frac{\rho_o C_v (\gamma-1)}{\alpha_{22}} \partial_t S_{22} = \frac{dQ}{dt}$$

$$= -\frac{1}{8\pi} T_o (\partial_T \nu_{11}) \partial_t D_1^2 \qquad \text{(A-33)}$$

The second term on the left is negligible on the time scale of the experiment. The right hand side is (again) the electrocaloric term which is negative when pulses get <u>into</u> the crystal, i.e., $\partial_t^2 D_1 > 0$ and positive when pulses <u>leave</u> the crystal, i.e. $\partial_t^2 D_1 < 0$. This effects no heat deposit in the crystal for a long enough time. Moreover, for short times after excitation pulses passage through the crystal, the driving terms in equations (A-32) and (A-33) vanish, and one ends up with solutions similar to those obtained in equation (A-29). Consequently,

the intitial heating dumped into the crystal has not been accounted for, yet.

It is proposed [36] to add a term proportional to D_1^2 and to absorption coefficient to the right hand side of equation (A-33). Also, the term in D_1^2 should be attributed to stimulated scattering and not to absorption. Nevertheless, the electrostrictive approach still stands deficient to account for the initial static term, and more should be known about the electromagnetic-acoustic coupling.

An acoustic-wave grating arises from a change in the number density N_j and changes in the positions of the resonances ω_j [38] with the former being predominant. A change δN is induced by an acoustic strain $S = \delta N/N$. Then, using equation (44), one obtains

$$2\Delta n_{ac}\ (\omega;\ \delta N) = \frac{dn}{dN_o}\ \Delta N_o = -\Delta S\ \left(\frac{n_o^2 - 1}{2n_o}\right) \qquad \text{(A-34)}$$

Where ΔN and ΔS are, respectively, the peak-null differences in number density and strain. Similarly, with the mere contribution of the origin(peak)

$$2\Delta\alpha_{ac}\ (\omega;\ \delta N) = \frac{d\alpha}{dN_o}\ \Delta N_o = \alpha_o(\omega)\ \frac{\Delta N}{N} = -\Delta S\ \alpha_o(\omega) \qquad \text{(A-35)}$$

Moreover, if spectral shifts are assumed to be linear with density, then

$$\Delta\omega_o = \phi\ \Delta S$$

where ϕ measures the interaction between the electronic energy level and

the acoustic phonon, and $\Delta\omega_o$ is the peak-null difference in ω_o. Then

$$2\Delta n'_{ac}(\omega;\ \Delta\omega_o) = \frac{dn}{d\omega_o}\,\Delta\omega_o$$

$$= \frac{2\phi\Delta S\ [\gamma_o^2 - 4(\omega_o - \omega)^2]\ \alpha_o^2(\omega)}{\gamma_o^3\ \alpha_o\ (\omega_o)} \qquad \text{(A-36)}$$

and

$$2\Delta\alpha'_{ac}(\omega;\ \Delta\omega_o) = \frac{-8\phi\Delta S\ (\omega_o - \omega)\ \alpha_o^2\ (\omega)}{\alpha_o\ (\omega_o)\ \gamma_o^2} \qquad \text{(A-37)}$$

where $\alpha_o(\omega_o)$ is the maximum absorption and is given by

$$\alpha_o\ (\omega_o) = \alpha_o(\omega = \omega_o) = \frac{1}{2n_o}\frac{N_o f'_o}{\gamma_o \omega_o} \qquad \text{(A-38)}$$

Terms in equations (A-35) - (A-37) are usually not observed and one can write the expression for acoustic diffraction efficiency (cf. equation (39)) as

$$\eta_{ac}(\omega) = e^{-2\bar{\alpha}\xi}\ (\frac{\pi\xi}{\lambda})^2\ (\frac{-\Delta S(n_o^2 - 1)}{4\ n_o})^2 \qquad \text{(A-39)}$$

signifying a quadratic dependence on strain.

VITA

Ali Muhammad Ghazzawi

Candidate for the Degree of

Doctor of Philosophy

Thesis: LASER SPECTROSCOPIC STUDIES OF IONS IN SOLIDS

Major Field: Physics

Biographical:

Personal Data: Born in Beirut, Lebanon, May 4, 1953, the son of Muhammad and Hind Ghazzawi.

Education: Received Bachelor of Science degree in Physics from The American University of Beirut in June, 1978; received Master of Science degree from the same university in October, 1980; completed requirements for the Doctor of Philosophy degree at Oklahoma State University in December, 1984.

Professional Experience: Graduate Teaching Assistant, Department of Physics, The American University of Beirut, 1978-1980; Laboratory Instructor, Beirut University College, 1979-1980; Laboratory Instructor, The Haigazian College, 1980; Graduate Teaching Assistant, Department of Physics and Astronomy, Rutgers University, 1980-1981; Teaching Assistant, Department of Physics, Oklahoma State University, 1981-1982; Research Assistant, Department of Physics, Oklahoma State University, 1982-1984.